https://doi.org/10.5194/egusphere-2024-1900
Preprint. Discussion started: 15 July 2024

Valley floor inclination affecting valley winds and transport of passive tracers in idealised simulations

Johannes Mikkola[1], Alexander Gohm[2], Victoria A. Sinclair[1], and Federico Bianchi[1]

[1]Institute for Atmospheric and Earth System Research/Physics, Faculty of Science, University of Helsinki, Helsinki, Finland
[2]Department of Atmospheric and Cryospheric Sciences, University of Innsbruck, Innsbruck, Austria

Correspondence: Johannes Mikkola (johannes.mikkola@helsinki.fi)

Abstract. In mountainous regions, diurnal thermally-driven winds impact daily weather and air-quality. This study investigates how the inclination of idealised valleys affects these winds and the transport of passive tracers using high-resolution numerical simulations with the Weather Research and Forecasting (WRF) model. We explore a range of valley inclinations between 0 and 2.28 degrees, bridging the gap between previous studies on flat and moderately inclined (up to 0.86 degrees) idealised valleys and steeper (2-5 degrees) real Himalayan valleys. We find that in the inclined valleys during the daytime the up-valley winds penetrate deeper into the valleys and are strengthen, up to a critical angle beyond which the winds weaken. Flat-floored valleys exhibit the strongest night-time down-valley winds overall, but surface-based down-valley winds are more prominent in inclined valleys. Steeper valleys enhance the vertical transport of passive tracers, resulting in ventilation at higher altitudes compared to the flat-floored valley. Despite stronger overall tracer outflow in the flat valley, this occurs at lower altitudes, leading most of the ventilated tracers being accumulated in the lowest few kilometers of the atmosphere. Consequently, steeper valleys are more efficient in ventilating tracers to the upper troposphere, which would for example lead to higher potential for long-range transport. These findings underscore the critical role of valley geometry in shaping wind patterns and pollutant transport, providing valuable insights for improving transport modeling in mountainous regions.

https://doi.org/10.5194/egusphere-2024-1900
Preprint. Discussion started: 15 July 2024

1 Introduction

In mountainous areas, daily weather and air-quality are influenced by thermally-driven winds that flow up the valleys and slopes during the day and down during the night (Whiteman, 2000). Diurnal valley and slope winds form due to horizontal temperature gradients that develop due to topography-induced differential heating of the lowest part of the atmosphere. Although pollutants emitted near the surface can be trapped in the valley atmosphere for days (Whiteman et al., 2014), the daytime winds are efficient in transporting the mass (i.e. air pollution) to the free troposphere – also referred to as mountain venting (Serafin et al., 2018). Once in the free troposphere, aerosol can affect the climate, for example, by altering cloud formation (Gordon et al., 2017) and can be transported long distances (Henne et al., 2004) affecting regions far away from the actual emission location. Modelling these transport processes in the mountain valleys is demanding, especially on global scales (Rotach et al., 2014), as resolving them accurately requires at least kilometer-scale grid spacing in model simulations (Wagner et al., 2014).

Daytime up-slope winds are a result of buoyancy forcing, as the air near the heated slope surface is warmer than the air away from the slope at the same altitude (Vergeiner and Dreiseitl, 1987; Farina and Zardi, 2023). Above the up-slope wind layer forms a flow towards the valley center and descending motion at the valley center. Depending on the valley shape, the cross-valley circulation often consists of two or more vertically stacked cells separated by stable inversion layers (Wagner et al., 2015b). Similarly to the daytime counterpart, night-time down-slope winds form as the air near the cooling surface cools down and become denser than air away from the slope (Vergeiner and Dreiseitl, 1987). The cross-valley slope winds respond quickly to the thermal forcing from the heated or cooled sloped surface and thus develop and reach their maxima soon after sunrise / sunset (Vergeiner and Dreiseitl, 1987). Up-slope and down-slope winds are often referred to as *anabatic* and *katabatic winds*, respectively. In this article the terms *anabatic winds* refer to winds flowing up and *katabatic winds* to winds flowing down an inclined surface. This applies regardless of whether these are valley winds along an inclined valley floor or slope winds that flow in a cross-valley direction. Important factors for the development of the anabatic and katabatic winds regarding this study are the background stability and slope angle (Vergeiner and Dreiseitl, 1987, Eq. 5). Increased background stability and steeper slope angle would decrease the along-slope mass flux, hence result as weaker flow magnitude and flow depth.

Daytime plain-to-valley and up-valley winds in the along-valley direction form due to the temperature gradient which develops between the valley atmosphere and the air above the adjacent plain (Whiteman, 2000). The temperature gradient is traditionally explained by the concept of the topographic amplification factor (TAF; Zardi and Whiteman, 2013), also referred to as the valley volume effect. When two horizontal areas of the same size are considered, one above the plain and the other above the valley, both located at ridge height, the volume of the air below the area over the valley is smaller than over the plain. Given the same heat input on top of the volume as solar radiation the temperature changes in the valley volume will be greater. However, TAF is considered as the theoretical maximum for the heat deficit, as some of the heat is exported out of the valley volume by the cross-valley circulation (Schmidli, 2013). Using the same volume comparison but with surface cooling, the night-time down-valley winds and valley-to-plain winds form due to a reversed pressure gradient (Whiteman, 2000). The along-valley winds develop much slower than the cross-valley up-slope winds, as the driving pressure gradient force is based on the warming or cooling of the valley atmosphere, instead of the shallow layer near the slope surface.

https://doi.org/10.5194/egusphere-2024-1900
Preprint. Discussion started: 15 July 2024

The daytime cross-valley circulation is efficient in transporting mass (i.e. air pollution) up to the ridge height from the valley bottom and slopes (Serafin et al., 2018), where often most of the emission sources are located. Along-valley winds contribute to the horizontal transport by the larger scale air exchange between the valley atmosphere and the surrounding plains and within the different parts along the valley (Gohm et al., 2009). Bianchi et al. (2021) suggested the daytime up-valley winds play an important role for ventilation of biogenic aerosol out of a Himalayan valley at high altitudes. Using in-situ aerosol measurements in the Khumbu valley combined with Lagrangian transport modelling, they found that the daytime up-valley winds transported aerosol up to 5 km altitude within the valley volume, which was followed by ventilation into the free troposphere at the head of the valley. Transport of pollutants to the high altitudes within the Khumbu valley (Hindman and Upadhyay, 2002; Bonasoni et al., 2010) and into the free troposphere by the local valley circulation (Venzac et al., 2008) is identified by other studies in the past. Bianchi et al. (2021) suggested that the southern slope of the Himalayas could act as a large source of free tropospheric aerosol, as other valleys in the mountain range could also have similar ventilation processes. Mikkola et al. (2023) compared the daytime up-valley winds in the Khumbu valley to three other major valleys nearby. Based on their comparison of the up-valley wind characteristics, the other three valleys would also have the potential for ventilation. Differences in the modelled up-valley winds across these valleys were hypothesized to stem from differences in terrain geometry, particularly valley floor steepness.

The valley winds and their associated transport processes are sensitive e.g. to the valley geometry (i.e. width, depth, narrowing, inclination or curvature; Wagner et al., 2015a; Weigel et al., 2006), synoptic-scale winds and pressure gradients (Whiteman and Doran, 1993)), temperature stratification (vertical profile of temperature; Schmidli and Rotunno, 2015) and valley surface properties (i.e. albedo and surface roughness; Gohm et al., 2009). Effects of the valley geometry on the valley winds and transport processes in mountain regions have been studied in the past by numerous measurement campaigns and numerical modelling studies, using both real (e.g. Zängl et al., 2001; Weigel et al., 2006) and idealised (e.g. Li and Atkinson, 1999; Schmidli and Rotunno, 2015; Wagner et al., 2015b; Leukauf et al., 2017; Göbel et al., 2023) topographies. Although Wagner wrote as early as 1938 about *slope winds* that form above and flow *along* inclined valley floors (Whiteman and Dreiseitl, 1984), studies which investigate the effect of valley floor inclination on the up-valley winds are (to the authors' best knowledge) almost absent from the literature. Exceptions are Wagner et al. (2015a) and Mikkola et al. (2023).

Wagner et al. (2015a) studied the effect of along-valley topographic heterogeneity on the daytime up-valley winds and transport processes by means of idealised WRF-simulations (Weather Research and Forecasting model). Valley floor inclination was one of the topographic factors they varied systematically. Their valleys had constant ridge heights of 1.5 km and in their steepest case the valley floor was inclined at 0.86 degrees. With a constant ridge height, the inclination of the valley floor leads to reduced valley volume and would strengthen the valley volume effect. For example, in the steepest case of Wagner et al. (2015a), the valley volume reduced in half compared to a flat-floored valley. Wagner et al. (2015a) found the valley floor inclination to strengthen the up-valley winds by a combination of enhanced valley volume effect and additional buoyancy forcing along the inclined valley floor. For example, they found that the steepest valley floor inclination (0.86 degrees) enhanced the daytime up-valley winds by a factor of 3.0. However, they did not quantify the relative contribution of these two effects. Mikkola et al. (2023) compared four Himalayan valleys in high-resolution WRF-simulations. Parts of these valleys were

https://doi.org/10.5194/egusphere-2024-1900
Preprint. Discussion started: 15 July 2024

inclined between 2 to 5 degrees. They found that the steepest parts of the valleys were associated with both weak and shallow daytime up-valley winds. Mikkola et al. (2023) suggested the contradiction in their results to Wagner et al. (2015a) is caused by the notable difference in the topographies of the studied valleys. The Himalayan valleys studied by Mikkola et al. (2023) are much steeper than the idealised valleys in Wagner et al. (2015a) so the up-slope buoyancy forcing was suggested to have larger role than the valley volume effect in driving the up-valley winds. Also, the valley volume effect is not necessarily enhanced in the Himalayan valleys due to the valley floor inclination, as the valley ridges are inclined as well. When the height difference between the valley center and ridge lines stays constant along the valley, the volume of air does not change even though the valley topography would be tilted to an angle.

In this article, we study how the valley inclination affects the valley winds and transport of passive tracers out of idealised mountain valleys. We perform numerical meteorological simulations using WRF (Skamarock et al., 2019) with idealised topographies. Our simulations fill the gap between Wagner et al. (2015a) and Mikkola et al. (2023) by extending the range of valley inclinations to also include steeper valleys than what was used in Wagner et al. (2015a) and by tilting the valley ridges similar to in the Himalayan valleys studied in Mikkola et al. (2023). In addition, we study how the location of the tracer release affect the tracer ventilation. We study how changing the along and cross-valley location of the tracer release affects the transport of the tracer mass and at which altitude the tracer end up from valleys with different inclination.

First, the methodology including the model setup and data analysis methods is introduced in Section 2. The valley flows are described in Section 3.1 and the transport of the passive tracers are described in Section 3.2. The results are discussed and compared to previous studies in Section 4 and conclusions are given in Section 5.

https://doi.org/10.5194/egusphere-2024-1900
Preprint. Discussion started: 15 July 2024

2 Methods

2.1 Model setup

In this study, we use the Weather Research and Forecasting model (WRF) version 4.4.1 (Skamarock et al., 2019). For flux computation and online averaging we use a budget calculation tool WRFlux (Göbel et al., 2022), which is a fork of the original WRF available online (Github repository, Göbel, 2022). Data analysis methods are described in detail in Section 2.4. The WRF model domain has a size of 200 km in y-direction (along-valley) and 40 km in x-direction (cross-valley) and a horizontal grid spacing of 200 m. The model domain has 140 model levels with the lowest model level at 15 m above the surface and model top at 20 km height. The vertical model level spacing is less than or equal to 100 m below the height of 5 km and has a maximum value of 308.25 m (Supplementary Fig. A1). A w-Rayleigh damping layer with a depth of 8 km is applied at the model top. Lateral boundaries are symmetric in y-direction and periodic in x-direction.

WRF is run in LES mode which uses three-dimensional 1.5 order TKE (turbulent kinetic energy) closure for turbulence, 3rd order Runge-Kutta time-integration scheme, 5th order in horizontal advection and 3rd order in vertical advection of momentum and scalars. Microphysics are parameterised using WRF single-moment scheme (Hong and Lim, 2006, WSM6 scheme). Surface layer physics are parameterised using the Revised MM5 similarity theory (Jiménez et al., 2012).

The simulations are initialised at 06LT (local time) in the morning and run for 48 hours with a timestep of 2 seconds. Surface sensible heat flux, H, is prescribed to follow a daily cycle defined by

$$H(t) = \max\left(H_{\text{max}} \sin\left(\frac{2\pi}{24\ \text{hr}} t\right), H_{\text{min}}\right), \tag{1}$$

where t is time in hours since the simulation start, $H_{\text{max}} = 150\ \text{Wm}^{-2}$ and $H_{\text{min}} = -10\ \text{Wm}^{-2}$ (timeseries of H shown in Suppl. Fig. A2). Values of H_{max} and H_{min} are based on the real-case WRF simulations covering the Nepal Himalayas used in Mikkola et al. (2023). Wagner et al. (2015a) and Schmidli and Rotunno (2010) both used similar prescribed daily cycles of the sensible heat flux in their idealised valley simulations. Moisture flux and latent heat flux at the surface are described by the surface layer model although the surface sensible heat flux is prescribed. The domain is initialised with relative humidity of zero on all model levels. The model domain has homogeneous surface properties defined as evergreen needle-leaf forest (USGS 24-category land use table), following the dominant land use type in the Himalayan valleys studied in Mikkola et al. (2023).

The initial temperature profile of the simulation is based on a 40-year climatology of Decembers 1979-2019 in the Eastern Nepal Himalayas (26-28°N, 86-88°E) in ERA5 reanalysis (Hersbach et al., 2020). December is generally a favourable period for studying thermally-driven valley winds in the region due the frequent clear skies and strong diurnal temperature cycle (Bollasina et al., 2002; Bonasoni et al., 2010). The initial vertical profile of the ideal WRF simulations and the ERA5 long-term average profiles are shown in Suppl. Fig. A3. In our simulations, the initial state is defined using a base temperature of 295 K at 1000 hPa, a constant Brunt-Väisälä frequency of 0.11 s^{-1} and the horizontal wind components are set to zero.

https://doi.org/10.5194/egusphere-2024-1900
Preprint. Discussion started: 15 July 2024

2.2 Idealised topographies

The idealised topographies used in this study are shown in Fig. 1. The topographies are defined following Wagner et al. (2015a) and Schmidli and Rotunno (2010), with an addition for the along-valley inclination. The simulated cases consists of four different valley topographies and one slope experiment. The simulated valleys are 100 km long in the y-direction and have a cosine-shape in the x-direction with 20 km width (ridge-to-ridge) and 2 km depth (valley center to ridge height difference). The valleys differ from each other by the angle of the linear increase in the surface height in the y-direction. The slope experiment has the same domain size and a linear increase of the surface in the y-direction without the shape of a valley. The remaining half of the model domain in the y-direction is covered by a flat plain in all simulations. Using a notation where the valley center line across the center of the valley is located along $x = 0$ km and the ridge height of 2 km is reached at $y = 0$ km, the valley topographies are defined by

$$h(x,y) = \Big(R_s h_r(y) - h_c(y)\Big)\left(\frac{1}{2} - \frac{1}{2}\cos\left(\pi\frac{|x|}{S_x}\right)\right) + h_c(y), \tag{2}$$

where R_s is the valley depth, $h_r(y)$ is the along-valley height profile of the ridge, $h_c(y)$ is the along-valley profile of the valley center ($x = 0$) and S_x is half-width of the valley (also the length of the slope in x-direction). The along-valley height profile of the valley center, $h_c(y)$, is defined by

$$h_c(y) = \begin{cases} 0, & y \le 0 \\ \frac{F_e}{L_y} y, & y > 0 \end{cases} \tag{3}$$

where L_y is the length of the valley and F_e is the valley center height at the end of the valley ($y = L_y$). The along-valley profile of the ridges is defined by

$$h_r(y) = \begin{cases} 0, & y \le -S_y \\ \frac{1}{2} + \frac{1}{2}\cos\left(\frac{\pi}{S_y} y\right) & -S_y < y < 0\,, \\ 1 + \frac{F_e}{R_s L_y} y & y > 0 \end{cases} \tag{4}$$

where S_y is the length in the y-direction over which the ridges increase in height to their full depth of 2 km at the valley entrance.

The topography parameters for the simulated cases used in Equations 2–4 are given in Table 1. The only difference between the four simulated valleys is the along-valley inclination of the valley floor and ridges. One of the valleys has a flat valley center height and a constant ridge height of 2 km (referred as case FLAT; Fig. 1a). The other three valleys are inclined so that the height of the valley floors increase linearly to 1 km (referred as case I1; Fig. 1b), 2 km (case I2; Fig. 1c) and 4 km (case I3; Fig. 1d). In all of the valleys, the valley center to ridge height difference remains 2 km meaning that the valley shape in the cross-valley direction remains the same for all of the valleys in all of their parts. The slope experiment (referred as case SLOPE; Fig. 1e) is a 100 km long slope inclined to reach 2 km height. The valley topographies are motivated by the Himalayan valleys studied by Mikkola et al. (2023). The steepest case in our experiments, I3, is representative by inclination, width and depth of the Khumbu valley, which leads to the base of Mt. Everest.

https://doi.org/10.5194/egusphere-2024-1900
Preprint. Discussion started: 15 July 2024

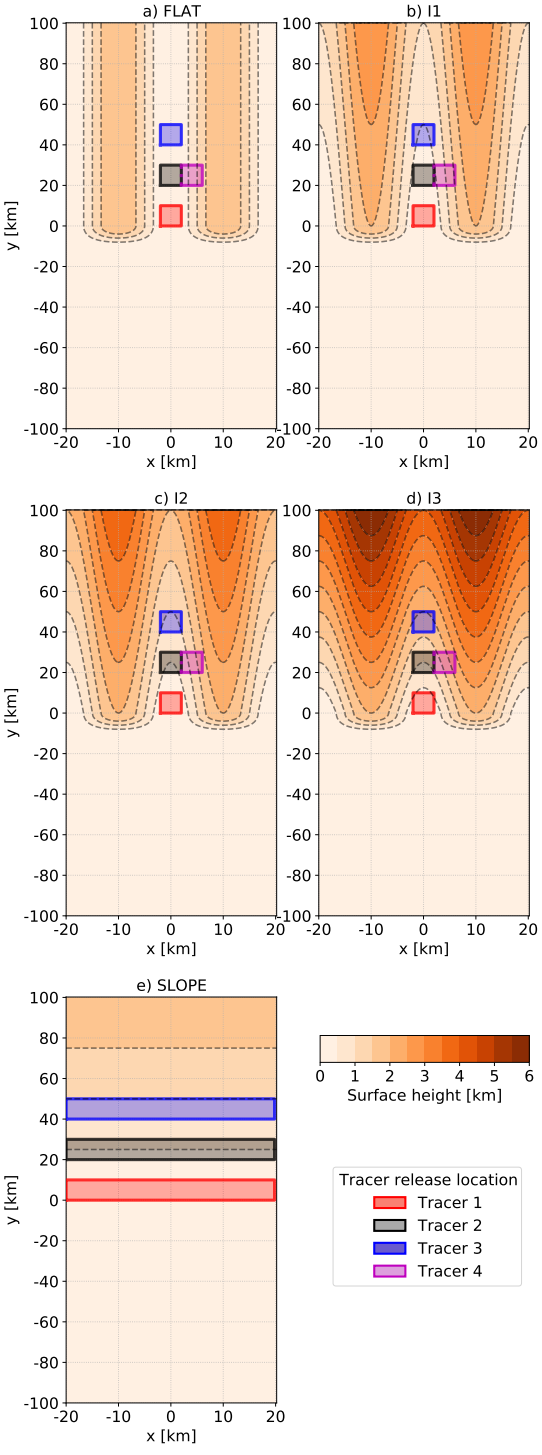

Figure 1. Model topography in cases **a)** FLAT **b)** I1 **c)** I2 **d)** I3 and **e)** SLOPE. Dashed lines show the topography on 500-m contours. Tracer release locations shown by color filled boxes.

https://doi.org/10.5194/egusphere-2024-1900
Preprint. Discussion started: 15 July 2024

Table 1. Topography parameters for Equations 2–4 in the simulated cases. Explanation for F_e, R_s, S_x and S_y is found in the main text. Values in the column "Inclination" are the tilt of the valley floors and ridges in along-valley direction between $y = 0...100$ km, i.e. $\arctan(F_e/100\ \text{km})$.

Case	Inclination [°]	F_e [km]	R_s [km]	S_x [km]	S_y [km]
FLAT	0	0	2	10	12
I1	0.57	1	2	10	12
I2	1.14	2	2	10	12
I3	2.28	4	2	10	12
SLOPE	1.14	2	0	0	0

2.3 Passive tracers

Transport processes are studied using passive tracers. In order to study the importance of the emission location, four passive tracers are released at different along-valley and cross-valley locations. Implementation of the passive tracers is done following the model setup by Lang et al. (2015). Tracer release locations are shown by color in Fig. 1 and in Suppl. Tables A1–A2. Three along-valley locations (0 km $< y <$ 10 km, 20 km $< y <$ 30 km and 40 km $< y <$ 50 km) are selected around the valley center line (-2 km $< x <$ 2 km) and one location on the right-hand side slope (20 km $< y <$ 30 km, 2 km $< x <$ 6 km). In the case SLOPE there are three tracers released in the same along-valley locations as in the valley simulations, spanning the whole model domain in the x-direction (Fig. 1e). The passive tracers are released in the six lowest model levels, which corresponds to an approximately 100 m deep surface-based layer. Technically the release happens by the addition of 1.0 g kg^{-1} to the tracer mixing ratio in the selected grid boxes every model timestep during 09:00–10:00 on the first morning of the simulation. Since the same number of grid boxes and model levels are used in the release for all of the valley topographies, the total tracer mass differs between the cases and tracers. As the release location is elevated along the inclined valleys but the released tracer mixing ratio is constant, the total tracer mass vary due to changes in the air density. Therefore, relative tracer mass and concentrations normalised by the total tracer mass in each simulation domain are shown in the analysis.

2.4 Data analysis

The analysis volumes are shown by the dotted lines in Fig. 2 for the topography I3. In the analysis, the valley volume is referred to as the whole length of the valley ($y = 0$ km to 100 km), ridge-to-ridge in the cross-valley direction ($x = -10$ km to 10 km) and below the ridge-height in the vertical. The lower half of the valley is the volume between $y = 0$ km to 50 km and the top half of the valley is between $y = 50$ km to 100 km. The wind and tracer analysis considers mainly the valley at the center ($|x| < 10$ km), in which the passive tracers are released. An identically shaped valley is located at $|x| > 10$ km (Fig. 1a-d), as the periodic boundary condition in x-direction join the two valley halves between the main valley and the domain

https://doi.org/10.5194/egusphere-2024-1900
Preprint. Discussion started: 15 July 2024

boundaries. This parallel valley is not included in the analysis if not clearly mentioned in the text. For the SLOPE case, the reference analysis volume is a 2-km deep layer above the sloped surface, which corresponds to the ridge height of the valley topographies, and the whole domain in x-direction.

Tracer fluxes at the ridge height and at the valley entrance are computed using WRFlux v.1.4.1 (Github repository, Göbel, 2022) which is a budget calculation tool for WRF. Using WRFlux one can output the time-averaged fluxes decomposed into resolved and sub-grid-scale components transformed into Cartesian coordinates (Göbel et al., 2022). Other tendency terms are also available but we use only the mean-flow and sub-grid-scale flux components in the analysis. Flux computation for the passive tracer fields were added to WRFlux v1.4.1 following the computation of the moisture flux (water vapor mixing ratio flux). Hourly averaged tracer fluxes in x-y-z directions for mean-flow and sub-grid-scale components are used in the analysis.

Arrows F1–F3 in Fig. 2 show the flux components considered for the passive tracers. F1 is the horizontal transport into / out of the volume at the valley entrance. F2 and F3 are the flux of tracers through the upper lid of the valley volume at the ridge height in the lower half and upper half of the valley, respectively. F2 and F3 are normal to the valley inclination meaning they consider not only the vertical tracer flux but also the y-direction of the tracer flux through the upper lid of the valley volume at the ridge height. For the case SLOPE the flux components are the same as shown by F1–F3 but they consider in x-direction the whole domain due to homogeneity of the slope.

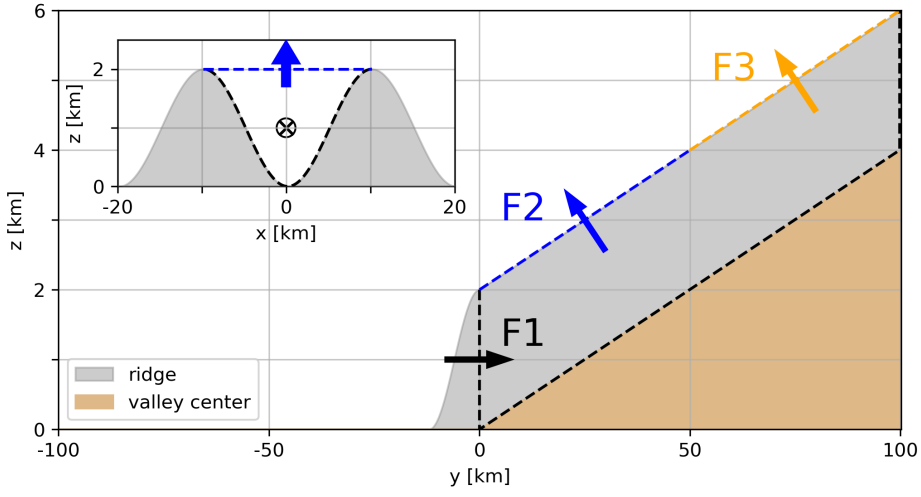

Figure 2. Flux components F1–F3 referred in the analysis (case I3 topography shown). In cross-valley direction F1 covers the whole valley ridge-to-ridge cross-section area and F2–F3 cover the whole width of the valley at ridge-height (shown in the sub-figure).

https://doi.org/10.5194/egusphere-2024-1900
Preprint. Discussion started: 15 July 2024

3 Results

3.1 Valley winds

In this section, the wind fields of the five simulations are described and compared. First, in sections 3.1.1–3.1.3 the spatial structures of the valley winds are analyzed, which is followed by a description of the temporal evolution in Section 3.1.4. The valley circulation comparison is summarised with time and volume integrals in Section 3.1.5. For clarity, the case SLOPE is always compared to the valley simulation I2 (which has the same inclination) separately from the comparison between the valley simulations.

3.1.1 Spatial structure of the wind and potential temperature during day 1

Figures 3 and 4 show the vertical cross-sections along the valley centers (along $x = 0$ km, left column) and across the half-way point of the valleys (across $y = 50$ km, right column). Fig. 3 shows the average for 15:00–16:00 on the first day and Fig. 4 for 03:00–04:00 on the first night. The same figures but for the second day and night are shown in Suppl. Figures A4 and A5, respectively.

Daytime up-valley winds and plain-to-valley winds form in all the simulations (Fig. 3). On the first day the convective boundary layer (CBL) over the plain, in which the plain-to-valley winds flow, grows up to 1.5 km above the surface ($y < 0$ km in Fig. 3a,c,e,g). The valley cases FLAT, I1, I2 and I3 show a typical isentropic structure associated with up-valley winds (Figures 3a,c,e,g). The CBL in the valley warms up more than the CBL above the plain which is seen as the isentropes turning towards the surface from the inversion top of the CBL in the valley. The along-valley circulation consists of single or multiple cells, varying between the valleys. Down-valley directed return flow of the main circulation cell is located right above the inversion top of the surface-based up-valley wind layer. A typical near-surface structure for isentropes associated with anabatic up-slope winds is seen in the cross-valley direction (Fig. 3b,d,f,h) but also in along-valley direction in the inclined valleys (Fig. 3c,e,g). The near-surface layer of air warms more than the air at the same altitude but located away from the slope, which is seen as a sharp turn of the isentropes downwards near the surface.

Two abbreviations for the convective boundary layer in the simulations are introduced for clarity and used hereafter. CBL_v refers to the surface-based unstable / neutral layer in the valley in which the up-valley winds flow, hence the layer with the strongest up-valley winds (dark red in Fig. 3). The depth and absolute height of the CBL_v changes along the valleys and evolves through the course of the diurnal cycle. CBL_p refers to the surface-based unstable / neutral layer above the plain in which the plain-to-valley winds flow. CBL_p has about constant depth throughout the plain but changes in time. For example, on the first day between 15:00-16:00 the CBL_p depth is about 1.5 km (Fig. 3). CBL_v and CBL_p are used in this study to qualitatively describe the valley's temperature distribution, not as quantitative measurements.

https://doi.org/10.5194/egusphere-2024-1900
Preprint. Discussion started: 15 July 2024

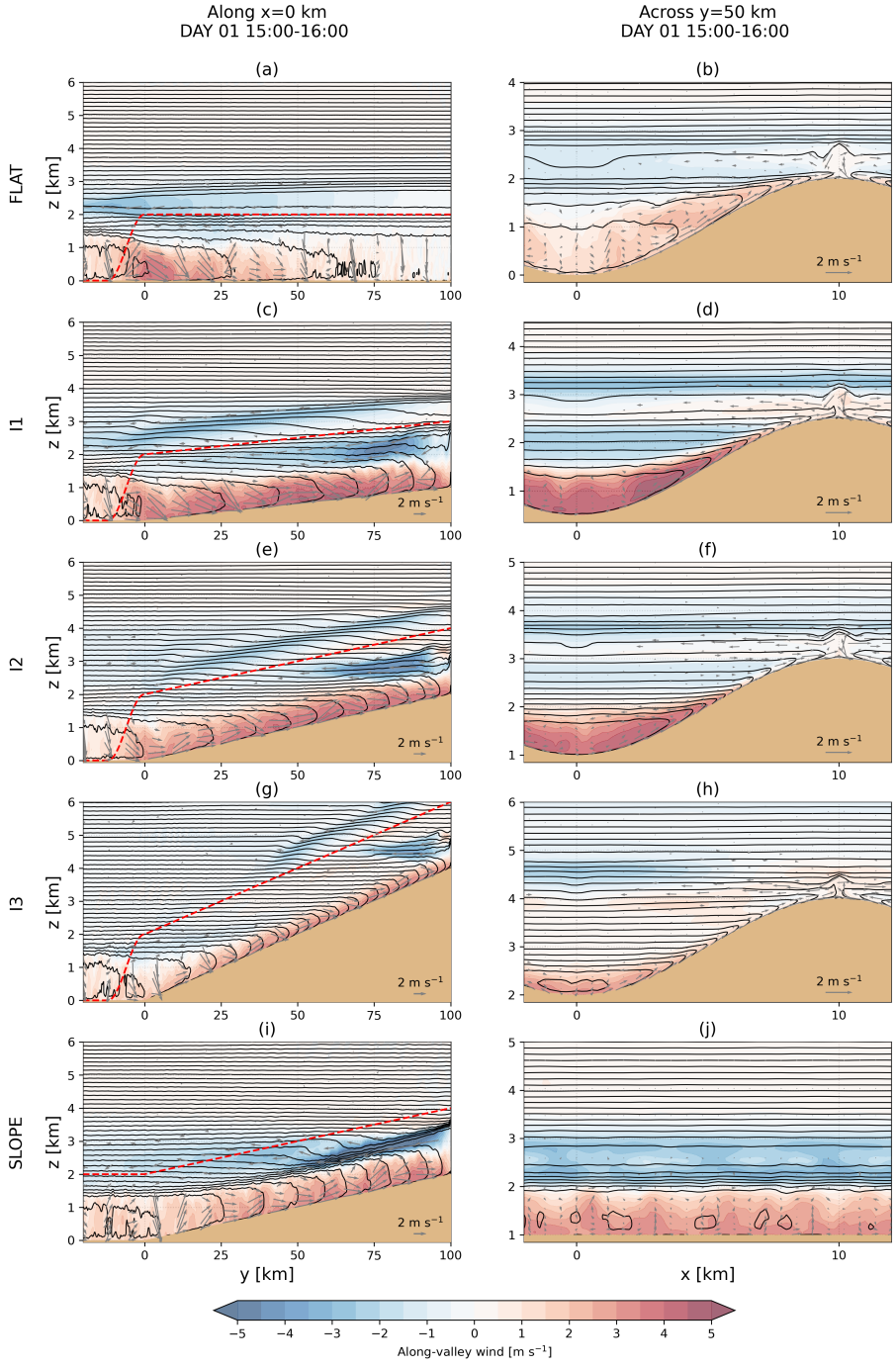

Figure 3. Vertical cross-sections along the domain centers at $x = 0$km on the left column (panels a,c,e,g,i) and across the domain at $y = 50$ km on the right column (panels b,d,f,h,j). For all panels the along-valley wind is shaded (positive for up-valley wind, 0.5 m s^{-1} interval) and potential temperature is plotted on contours (0.5 K interval). Grey vectors show the wind component in the plotted plane. The plotted values are an hourly average of 15:00–16:00 on the first day of the simulation.

https://doi.org/10.5194/egusphere-2024-1900
Preprint. Discussion started: 15 July 2024

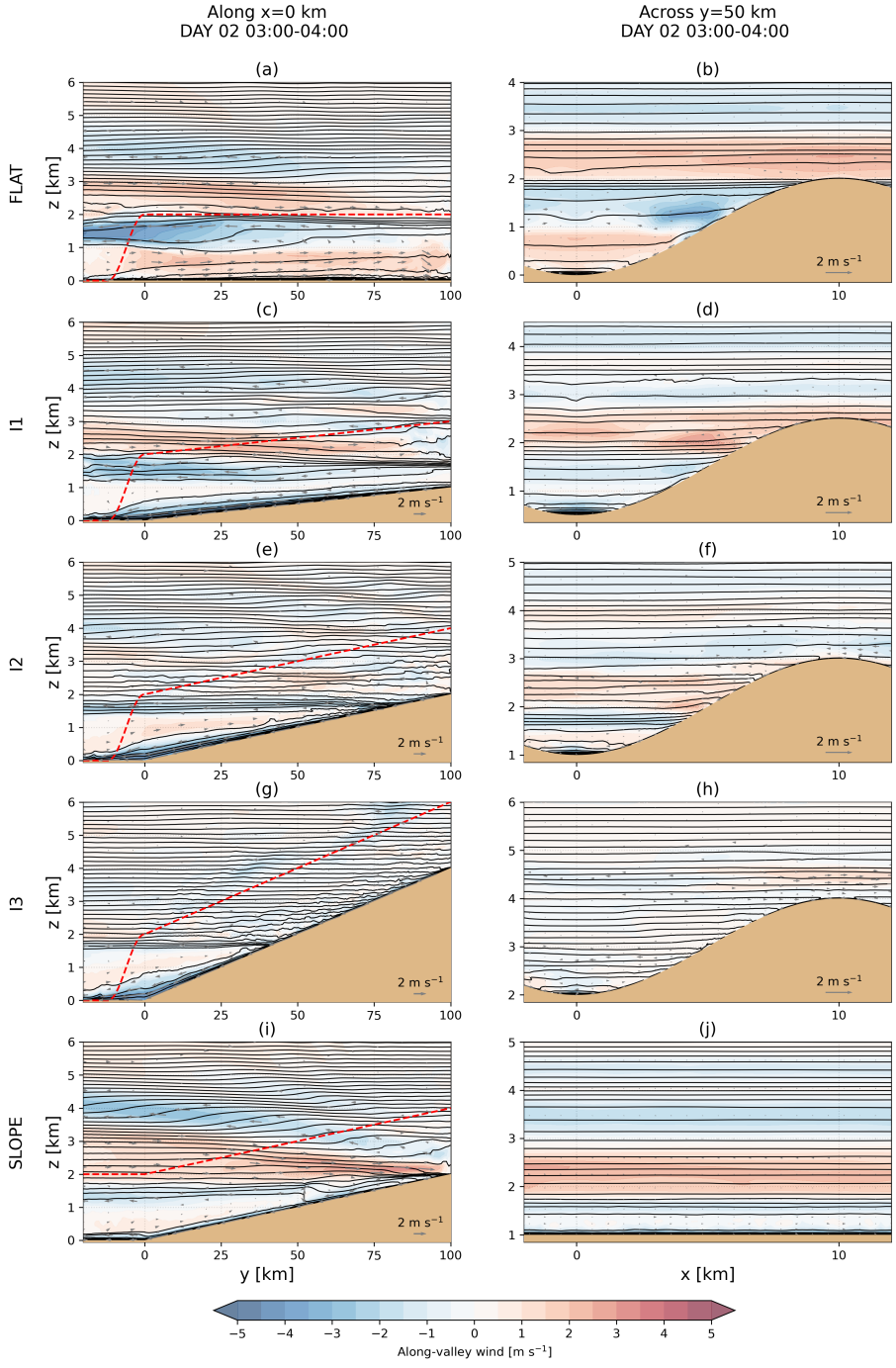

Figure 4. Same as Fig. 3 but for 03:00–04:00 on the first night of the simulation.

https://doi.org/10.5194/egusphere-2024-1900
Preprint. Discussion started: 15 July 2024

A few major differences in the daytime valley circulation between the simulations were identified in the along-valley cross-sections (Fig. 3a,c,e,g):

- The up-valley winds penetrate further up into the inclined valleys when compared to the case FLAT,
- within the inclined valleys the up-valley winds become weaker and shallower with increasing inclination,
- inclined valleys have multiple circulation cells in the along-valley direction where as the case FLAT only has one circulation cell.

These differences are described in details in the following paragraphs.

The daytime up-valley winds reach further up into the inclined valleys (Fig. 3c,e,g) compared to the case FLAT (Fig. 3a). In case FLAT the strongest up-valley winds are found near the valley entrance which is followed by weaker winds further in the valley. Near the valley entrance the maximum up-valley winds speeds reach up to 3.5 m s^{-1} and decreases down to less than 1.5 m s^{-1} within the first 25 km at the valley center $x = 0$ km (at 15:00-16:00 on the first day of the simulation, Fig. 3a). At the head of the valley ($y > 75$ km), the along-valley winds are less than 0.5 m s^{-1}. In the inclined valleys the up-valley winds reach the head of the valley with almost constant strength along the valley (Fig. 3c,e,g) but with decreasing up-valley wind speed with increasing inclination. The up-valley wind speeds reach up to 4 m s^{-1} in case I1 (Fig. 3c), 3.5 m s^{-1} in case I2 (Fig. 3e) and up to 3 m s^{-1} in case I3 (Fig. 3g). In the inclined valleys, near the surface, a similar isentrope structure in the along-valley direction to what would typically be associated with anabatic up-slope winds is found. This suggests that the buoyancy-driven anabatic winds are contributing in the daytime to the up-valley winds near the surface. This is caused by the inclined heated valley surface which likely causes horizontal temperature gradient in along-valley direction not only in the valley entrance region as in FLAT but continuously along the whole inclined valley as also typical for up-slope winds.

Near the valley entrance the flow depth of the up-valley winds is same for all the valleys (Fig. 3a,c,e,g) and corresponds roughly to the depth of the CBLp (1.5 km in Fig. 3a,c,e,g). Further up in the valleys, the flow depth decreases with increasing valley inclination. The depth of the up-valley wind layer is limited from above by the capping inversion of the CBLv. The CBLv depth varies with location within the valleys. Above the CBLv, away from the heated valley surface, the atmosphere is stably stratified. In case FLAT the CBLv depth slightly decreases along the valley (Fig. 3a) whereas in all other valleys it strongly decreases (Fig. 3c,e,g). This implies that in most inclined valleys a large portion of the valley atmosphere is stably stratified. This fraction increases with increasing inclination. In the inclined valleys the height of the CBLv decreases to a constant depth, which also decreases with increasing inclination of the valley. Near the head of the valley where the up-valley winds encounter the domain boundary, the CBLv depth changes (discussed later in this section).

The along-valley circulation in the valleys consist of singular circulation cell in case FLAT (Fig. 3a) and multiple cells in the inclined valleys (Fig. 3c,e,g). The along-valley and vertical location of the down-valley directed return flow of the main circulation cell varies between the valleys. Here the term main circulation cell refers to the surface-based up-valley wind layer in CBLv and the strongest return flow directly above it. In the case FLAT, the return flow is located mostly above the valley volume around the altitude of 1.5 to 3 km and it is strongest above the valley entrance ($|y| < 10$ km, Fig. 3a). In the inclined

https://doi.org/10.5194/egusphere-2024-1900
Preprint. Discussion started: 15 July 2024

valleys, the return flow is located mostly inside the valley volume with varying altitudes due to the elevation along the valleys (Fig. 3c,e,g). The strongest wind speeds in the return flow are found near the head of the valley ($y > 75$ km) and vertically in the upper 1 km of the valley volume. The altitude of the return flow in the inclined cases is between 2 and 3 km for case I1 (Fig. 3c), between 2.5 and 3.5 km for case I2 (Fig. 3e) and between 4 and 5 km for case I3 (Fig. 3g). The strong return flow near the head of the valley in the inclined valleys is likely caused by the symmetric boundary conditions that lead to forced convergence near $y = 100$ km. Driven likely by the buoyancy force generated by the heating of inclined valley floors, up-valley winds extend all the way to the y-boundary at the head of the valley.

A secondary circulation cell in the along-valley direction forms in the inclined valleys, clearly present only in cases I1 (Fig. 3c-d) and I2 (Fig. 3e-f). The secondary circulation cell is shallower and weaker than the main circulation cell and it is located above the ridge height. That this circulation forms only above the inclined valleys and not in the case FLAT is likely related to the elevated near-neutral / less stable layer which is found around the ridge height (Fig. 3b,d,f,h). The near-neutral layer around the ridge height is the most pronounced in the case FLAT (Fig. 3b), with decreasing presence with increasing inclination (Fig. 3d,f,h). These elevated layers likely form due to the subsidence warming in the valley core and the diverging horizontal flow from the ridge-tops ($x = \pm$ 10 km) towards the valley center (Schmidli, 2013). The elevated warmed layer gets weaker with increasing valley inclination likely due to weakening cross-valley circulation. The elevated near-neutral layer is located around the ridge height for each along-valley point (i.e. along y-coordinate) of the valley. For the inclined cases the altitude of this layer increases along the valleys (Fig. 3c,e,g). Now, along the whole length of the valley, the elevated near-neutral layer is warmer than the air at the same altitude towards the plain. This temperature gradient is likely to form the secondary circulation cell in the along-valley direction. This secondary cell does not form in the case FLAT since the elevated near-neutral layer is at the same altitude for each along-valley point of the valley ($z \approx 2.5$ km, Fig. 3a).

Similarly to the inclined valley cases, in the case SLOPE the daytime plain-to-slope winds are limited between the sloped surface and the inversion top of the local CBL (Fig. 3i). The plain-to-slope winds are weaker than in case I2 especially at the beginning of the slope ($y = 0$ km) which corresponds to the valley entrance of I2. The along-valley circulation consists of one prominent cell in case SLOPE. The down-valley return flow in the case SLOPE is much stronger and shallower and is located below the 2 km reference height. In the x-direction, there is nothing in particular happening in the case SLOPE as the slope is homogeneous in this direction and the variation in the flow field is very small.

3.1.2 Spatial structure of the wind and potential temperature during day 2

On the second day of the simulation (Suppl. Fig. A4), the patterns of plain-to-valley and up-valley winds are very similar to those simulated on the first day. Up-valley wind speeds are not notably different between the first (Fig. 3) and second day (Suppl. Fig. A4) at 15:00-16:00 in the afternoon. The main difference between the two days is the deeper plain-to-valley and up-valley winds on the second day which implies also deeper CBL_p and CBL_v. The larger magnitude of the prescribed surface sensible heat flux during daytime than during night-time results in a net heating of the boundary layer during the course of a full daily cycle, which explains the deeper CBL on the second day (2 km, Suppl. Fig. A4a,c,e,g) than on the first day (1.5 km, Suppl. Fig. 3a,c,e,g).

https://doi.org/10.5194/egusphere-2024-1900
Preprint. Discussion started: 15 July 2024

Since the surface based up-valley winds flow in a deeper layer on the second day, also the return flows are located higher up. In the case FLAT the return flow is located completely above the valley volume (Suppl. Fig. A4a,b). In the inclined cases I1–I3 the return flow is also located higher but still below the ridge height in the valley volume (Fig. A4c,e,g). The spatial extent of the return flow is similar to that on the first day, but the secondary circulation cells are much more prominent on the second day with stronger wind speeds.

3.1.3 Spatial structure of the wind and potential temperature during night-time

The night-time along-valley winds in the simulations consist of three major components, which are surface-based down-valley winds and up-valley winds in the residual layer with associated down-valley return flow (Fig. 4). In addition, a secondary circulation with weak up- and down-valley directed winds form above the valley volumes.

Surface-based down-valley winds form in all of the valleys (Fig. 4). In case FLAT this down-valley wind layer is less than few tens of meters deep and the wind magnitude is less than 0.5 m s^{-1} (vertical profiles shown in Suppl. Fig. A7). At the valley exit ($y = 0$ km) in the inclined valleys, the surface-based down-valley winds have a maximum wind speed around 4 m s^{-1} at the height of 100 m and the wind turns up-valley at around the height of 600 m. The surface-based down-valley winds in the inclined valleys are likely intensified by the katabatic wind mechanism acting along the cooled valley slopes. Strong inversions form in the valleys I2 and I3 at the same altitude as the top of the residual layer at the plain and above this altitude the atmosphere is stably stratified (Fig. 4e-h). The inversion forms also in the cases FLAT and I1 but having similar strength only near the head of the valleys. In the stably stratified part of the valleys I2 and I3 the surface-based katabatic down-valley winds flow in a shallow layer of less than 100 meters (Suppl. Fig. A7). This could be explained by the katabatic wind strength and depth being inversely proportional to the background stability (e.g., Vergeiner and Dreiseitl, 1987, Eq. 5), hence the katabatic down-valley winds in the near-neutral residual layer are stronger and flow in a deeper layer.

During night-time there are up-valley winds in the core of the valley volumes above the aforementioned surface-based down-valley winds (Fig. 4). A down-valley return flow is found below the inversion capping the residual layer, which maintains a relatively constant altitude from the plains into the valleys. This circulation dominates spatially the night-time along-valley winds in case FLAT and has a decreasing role with increasing inclination. The residual layer in the valley volume remains warmer than the air above the plain at the same height which is likely the reason for these up-valley winds. After the surface heating turns into cooling at 18:00, the strongest up-valley winds from the entrance in the case FLAT start spreading further up into the valley, eventually reaching the head of the valley (Fig. 4a). In the case I1 (Fig. 4c) these winds extend up to the head of the valley (y=100), but in the steeper valleys I2 (Fig. 4e) and I3 (Fig. 4g) the along-valley extent is limited to the distance where the valley floor reaches the height of the top of the residual layer. In the inclined valleys the surface-based down-valley winds occupy a deeper layer and which leaves less space in the valley atmosphere for the residual layer (Fig. 4c,e,g).

Case SLOPE has night-time up-slope directed winds in the residual layer (Fig. 4i). In the case SLOPE these up-slope winds and the down-slope return flow are weaker than in the case I2 (Fig. 4e). Katabatic down-slope winds also form in the case SLOPE (Fig. 4i) but they are weaker and shallower compared to the case I2 (Fig. 4e). The additional down-slope winds towards the valley center in cross-valley direction likely enhance the strength and depth of the katabatic down-valley winds at

https://doi.org/10.5194/egusphere-2024-1900
Preprint. Discussion started: 15 July 2024

the valley center (x = 0 km) in the case I2. The strong step in the isentropes in case SLOPE around $y = 50$ km resembles a hydraulic jump which forms in the boundary of the residual layer and its' inversion top. Similar flow structures in katabatic winds are identified for example in Yu et al. (2005).

The second night of the simulation (Suppl. Fig. A5) has similar flow structures as the first night. The inversion top is located higher up, which gives more volume and along-valley distance for the up-valley winds in the residual layer and their associated return flow to develop in. The increased inversion height also means that the katabatic down-valley winds in the inclined valleys obtain a deeper flow depth at the valley entrance due to the longer along-valley distance between the inversion and the valley entrance. In addition, the secondary circulation cell located above the inversion is stronger during the second night.

3.1.4 Temporal evolution of the spatially averaged along-valley winds

Timeseries of the valley volume averaged along-valley wind speed for each case are shown in Fig. 5a. The averaging volume for case SLOPE is a 2-km deep layer above the sloped surface. Down-valley directed return flows that are located within the valley volumes have a huge impact on the valley averaged daytime along-valley winds. Since we are particularly interested in the daytime up-valley winds and their potentially crucial role in the transport of tracers from the valley atmosphere to the free troposphere, we also show the averaged up-valley wind component in Fig. 5b. In this latter case, only positive values of the along-valley wind component are averaged, which avoids compensation due to negative values associated with the return flow.

A daily cycle of up-valley winds during the day and down-valley winds during the night forms in all of the simulations (Fig. 5a). There is a clear difference in the along-valley wind magnitudes between the simulations and the two simulated days. On the first day, the maximum magnitudes of the valley averaged up-valley winds vary between 1 m s^{-1} and 3 m s^{-1} (Fig. 5b). The strongest up-valley winds are found in case I1 and the weakest in the case I3 which is in agreement with the Fig. 3 discussed in Section 3.1.1. Magnitudes of the night-time down-valley winds decrease with increasing inclination. On the second day, the case FLAT has just slightly higher maximum up-valley winds, but the difference to I1 is less than 0.1 m $s^{-}1$ (Fig. 5b). When considering the averaged along-valley wind, including also the negative values in Fig. 5a, one would conclude that the case FLAT has clearly the strongest up-valley winds. This difference is caused by the down-valley directed return flow which is located mostly outside the valley volume in the case FLAT (section 3.1.1) and hence does not impact the valley volume average as much as in the inclined cases.

In steeper valleys, the daytime up-valley wind speed (Fig. 5b) more closely follows the temporal evolution of the surface sensible heat flux (Suppl. Fig. A2). The time of maximum up-valley wind speed varies across cases, ranging from 13:00 for case I3 to 21:00 for case FLAT. This indicates that steeper valleys (like case I3) experience the most intense up-valley winds earlier in the day. Similarly, with increasing inclination the night-time down-valley winds form and peak earlier. This time difference could be explained by the response timescale of the anabatic up-valley winds compared to the valley volume effect driven up-valley winds (Vergeiner and Dreiseitl, 1987). The plain-to-valley winds are driven by the pressure gradient which forms between the CBL_v and CBL_p. Anabatic winds flow in a shallower layer and require shorter time to build up to the same magnitude in wind speed. This is the reason for the anabatic up-valley winds forming shortly after the beginning of the surface heating, seen as stronger up-valley winds in the inclined valleys during the morning hours (Fig. 5b). The response timescale

https://doi.org/10.5194/egusphere-2024-1900
Preprint. Discussion started: 15 July 2024

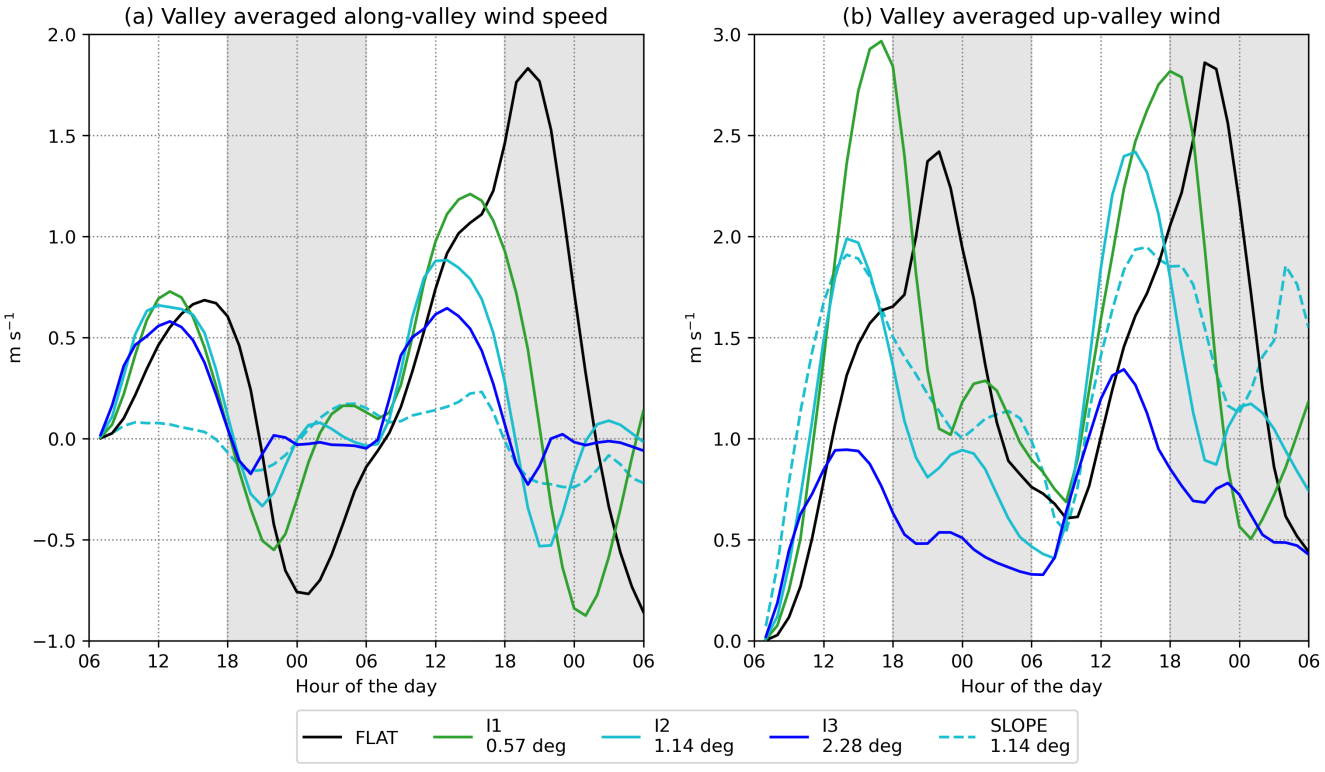

Figure 5. Timeseries of the valley volume averaged **(a)** along-valley wind speed **(b)** up-valley wind speed. Shown values are hourly averages plotted at the start of the averaged hour. Positive values refer to up-valley wind. For the valleys (cases FLAT, I1, I2, I3) the averaging volume is shown on dashed lines in Fig. 2. For the case SLOPE the averaging volume is a 2-km deep layer above the sloped surface. Timesteps with negative surface sensible heat flux are indicated by gray shading.

of the anabatic (and katabatic) winds is inversely proportional to the Brunt-Väisälä frequency and sine of the slope inclination (Schumann, 1990). The steeper the valley is inclined, the larger the share of its' volume of air is stably stratified due to the shallower CBLv, hence the Brunt-Väisälä frequency is larger. Both of these factors increase with valley inclination which explains the shorter response time during the morning and evening transition period for the steeper valleys.

On the second day, the valley volume averaged along-valley wind speeds are stronger compared to on the first day (Fig. 5a). However, the valley volume averaged up-valley wind speeds do not increase with the same proportion (Fig. 5b). On the second day, the up-valley winds flow in a deeper layer as the CBL_v grows deeper (Section 3.1.1–3.1.2). Due to the deeper up-valley winds, the return flow is mostly or partly located above the valley volume and thus has less of a contribution to the valley volume averaged along-valley wind speeds (Fig. 5a). Case I1 is the only simulation which does not show an increase in the up-valley wind speeds on the second day.

The night-time down-valley winds peak earlier in the night with steeper valley inclination (Fig. 5a). Furthermore the strength of the night-time down-valley winds decrease with increasing inclination. The down-valley return flows associated with the

https://doi.org/10.5194/egusphere-2024-1900
Preprint. Discussion started: 15 July 2024

remaining night-time up-valley winds in the residual layer occupy a smaller volume of the valley atmosphere for the steeper valleys (discussed in Section 3.1.3) which explains the weaker valley averaged down-valley winds. The earlier peak with steeper valley inclination would be explained by the response timescale discussed above.

In the volume averaged along-slope wind, the case SLOPE has much weaker winds compared to the case I2 (Fig. 5a). Its return flow is entirely located within the analysis volume (Section 3.1.1) which decreases the volume averaged up-slope wind drastically. The 2-km deep analysis volume in the case SLOPE was selected to correspond to the ridge-height in the valley simulations. When averaging only the positive along-slope winds, the strength of the flow in case SLOPE is comparable to that in case I2 (Fig. 5b). In the morning, winds in the case SLOPE are slightly stronger than in the valley simulations.

3.1.5 Along-valley air mass transport

Figure 6 summarises how the average along-valley air mass transport varies with valley inclination and the time period over which it is integrated. The shown variable is the averaged horizontal along-valley mass flux, integrated over four different time periods: (1) the whole 48 hours of the simulation (black circles), (2) when the valley volume averaged along-valley winds are positive (red squares), (3) times with non-negative surface sensible heat flux from 06:00 to 18:00 (blue triangles) and (4) times with negative surface sensible heat flux from 18:00 to 06:00 (purple crosses). Hereafter this variable is referred to as the air mass transport in the valley. See Appendix A for detailed explanation how the plotted variable in Fig. 6 is derived.

In general, the total air mass transport, which includes both the up and down-valley transport (i.e. the net horizontal transport) decreases with increasing valley inclination during daytime (Fig. 6a). Similar behaviour is also seen when only the positive (i.e. up-valley) mass transport is considered (Fig. 6b). However, this result is sensitive to the time period over which the air mass transport is integrated, particularly in the case FLAT. In this simulation, both the total air mass transport (Fig. 6a) and the positive air mass transport (Fig. 6b) are much lower when integrated over periods with positive surface sensible heat flux (blue triangles) compared to periods with positive averaged along-valley winds (red squares). This is because in the case FLAT the along-valley winds remain positive longer than the surface sensible heat flux is positive (Fig. 5a), which is presumably due to the longer response timescale of the valley volume effect driven up-valley winds than for the anabatic up-valley winds in the inclined cases. In contrast, for the inclined valleys, the along-valley wind component becomes negative around the time when the surface sensible heat flux turns negative. Therefore, for inclined valleys, the analysis period of positive along-valley winds (red squares) and the period of positive surface sensible heat flux 06:00–18:00 (blue triangles) in Fig.6a and Fig. 6b are similar.

https://doi.org/10.5194/egusphere-2024-1900
Preprint. Discussion started: 15 July 2024

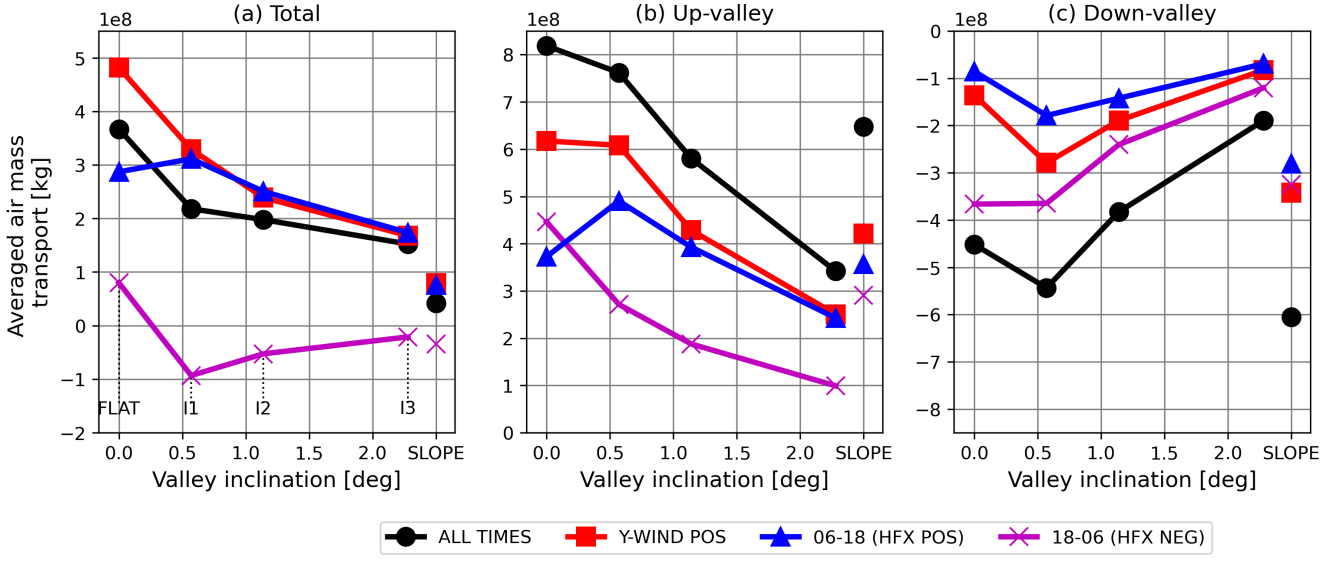

Figure 6. Time integral of the valley averaged **(a)** total y-component mass flux **(b)** positive y-component mass flux **(c)** negative y-component mass flux plotted against the valley inclination. For case SLOPE the averaging volume is a 2-km deep layer above the sloped surface. Four time periods are considered: (1) the whole 48 hour simulation plotted on black dots, (2) the timesteps with positive valley volume averaged along-valley wind plotted on red squares (timesteps when Fig. 5a is positive), (3) timesteps with non-negative surface sensible heat flux (06:00-18:00) plotted on blue triangles and (4) timesteps with negative surface sensible heat flux (18:00-06:00) plotted on purple crosses. Case SLOPE is plotted separately on the right-hand side of each panel. Due to the lack of sidewalls in case SLOPE, the values of SLOPE have been divided by 4 to have corresponding values with the valley simulations (see the sub-figure in Fig. 2, area within the dashed lines compared to the whole width below 2 km height).

The previous analysis suggests that a small inclination in the valley floor can enhance the daytime air mass transport, whereas a strong inclination reduces the air mass transport (06:00-18:00, blue triangles in Fig. 6b). Within our simulations the case I1 with the inclination of 0.57 degrees has the strongest daytime up-valley mass transport. We hypothesise that this is due to the contribution of the buoyancy force to the along valley winds. According to the theoretical model of Vergeiner and Dreiseitl (1987) for slope winds (their Eq. 5), the total mass flux of anabatic winds decreases with increasing surface slope and background stability. This would explain why the additional buoyancy forcing only increases the mass flux for shallow inclinations but not for steep ones. Moreover, the background stability, which determines the buoyancy forcing, is not the same in all simulations and also varies with height. Therefore, for small valley inclination (e.g., I1), the background stability is essentially determined by the CBL_p (Fig. 3c), implying weak stability. For strong valley inclination (e.g., I3), the stability is determined by the stably stratified atmosphere above the CBL_p (Fig. 3g), implying high stability. For intermediate inclinations (e.g., I2), there is a gradual transition from weak to strong background stratification as the valley winds pass the altitude of the CBL_p top. Consequently, a continuous decrease of the valley wind depth occurs along the valley (Fig. 3e), which aligns with the Prandtl model's prediction of an inverse relationship between the depth of the slope wind layer and the background stability

https://doi.org/10.5194/egusphere-2024-1900
Preprint. Discussion started: 15 July 2024

(e.g. Farina and Zardi, 2023, Eq. 10). In summary, the strongest valley winds may occur at an optimal valley inclination. This inclination maximizes the combined forcing of two factors: the valley volume effect, which arises from horizontal pressure gradients, and the slope flow effect, driven by buoyancy gradients.

The magnitude of the negative (i.e. down-valley) air mass transport during daytime decreases with increasing valley inclination for the inclined valleys (Fig. 6c). This means that the return flow during the day is weaker for steeper valleys, which from a mass conservation point of view is consistent with the positive mass flux which also decreases with increasing inclination. Although the flat valley appears to have a weaker return flow than the I1 case, this is only because the return flow in the flat case is above the 2-km deep averaging volume (Fig. 3a).

At night-time both the positive air mass transport and the magnitude of the negative air mass transport decreases with increasing valley inclination (purple crosses in Fig.6b, c). Noteworthy is that for the flat valley, the total mass transport remains positive (i.e. up valley) at night. This is caused by the strongest up-valley winds occurring in the evening which are much stronger during the second day compared to the night-time down-valley winds (Section 3.1.4).

https://doi.org/10.5194/egusphere-2024-1900
Preprint. Discussion started: 15 July 2024

3.2 Tracer transport

In this section the transport of tracers in the simulations is described. First, the temporal evolution of tracer mass within the valley atmospheres is described in Section 3.2.1. The location and timing of the tracer mass flux out of the valleys are described in Section 3.2.2 and the final tracer mass distribution in the model domain is described in Section 3.2.3. The tracer analysis in this section considers only the main valley located at the center of the domain ($|x| < 10$ km, Fig. 1) except in Section 3.2.3 where the parallel valley located at $|x| > 10$ km is taken into account as well.

3.2.1 Time evolution of tracer mass in the valleys

Figure 7 shows the timeseries of relative tracer mass in the valley volumes. The relative tracer mass is the ratio of the tracer mass in the valley volume to the total tracer mass in the domain. For the case SLOPE the reference volume is the 2-km layer above the sloped surface. The tracers are released in the first morning between 9:00–10:00 which is shown by the red shading.

The most intense transport of tracer mass out of the valleys happens during the first six hours after the tracer release (Fig. 7). During these six hours 30%–70% of the tracer mass is transported out of the valleys. Some of the tracer mass is re-injected back into the valley volumes mostly during night-time, which is seen as an increase of the relative tracer mass with time. The strongest contrast in the valley tracer mass between the case FLAT and the inclined valleys forms during the first night. During the first night the relative tracer mass decreases by 20%–35% in case FLAT. In the inclined valleys the relative tracer mass mostly stays approximately constant or changes less in magnitude compared to the case FLAT. Around 09:00 on the second day the valley tracer mass starts decreasing again in the inclined valleys, coinciding with the formation of the up-valley and up-slope winds. During the last six hours of the valley simulations the exchange of tracer mass between the valleys and their surroundings is very small.

The most notable difference within the four tracers is between the tracer 4 (Fig. 7d) and the other tracers 1-3 (Fig. 7a-c). Tracers 1-3 are released at the valley center ($|x| < 2$ km) whereas tracer 4 is released at the slope (2 km $< x <$ 6 km). For tracer 4, the transport out of the valley atmosphere during the first 6 hours is much more intensive since the tracer is released closer to the ridge height and also released directly into the cross-valley up-slope wind layer. However, the end result of the relative tracer mass in the valleys is almost the same for all of the tracers in each case.

The time evolution of the tracer mass within the reference volume differs a lot between the case SLOPE (dashed line in Fig. 7) and the valley simulation I2. During the first 24 hours after the tracer release, at most 20% of the tracer mass is transported out of the reference volume in the case SLOPE. Only during the second afternoon of the simulation SLOPE, a drastic drop of more than 40% in tracers 2 and 3 is seen. Strong re-injection of tracer mass back to the reference volume occurs for all of the tracers on the second night towards the end of the simulation.

3.2.2 Tracer flux out of the valleys

Figure 8 shows the timeseries of the flux components F1–F3 (see Section 2.4) for tracer 2 in the simulations. The same figure but for tracers 1, 3 and 4 are shown in Supplementary Figures A8–A10. Tracer 2 is shown here as it is released at the valley

https://doi.org/10.5194/egusphere-2024-1900
Preprint. Discussion started: 15 July 2024

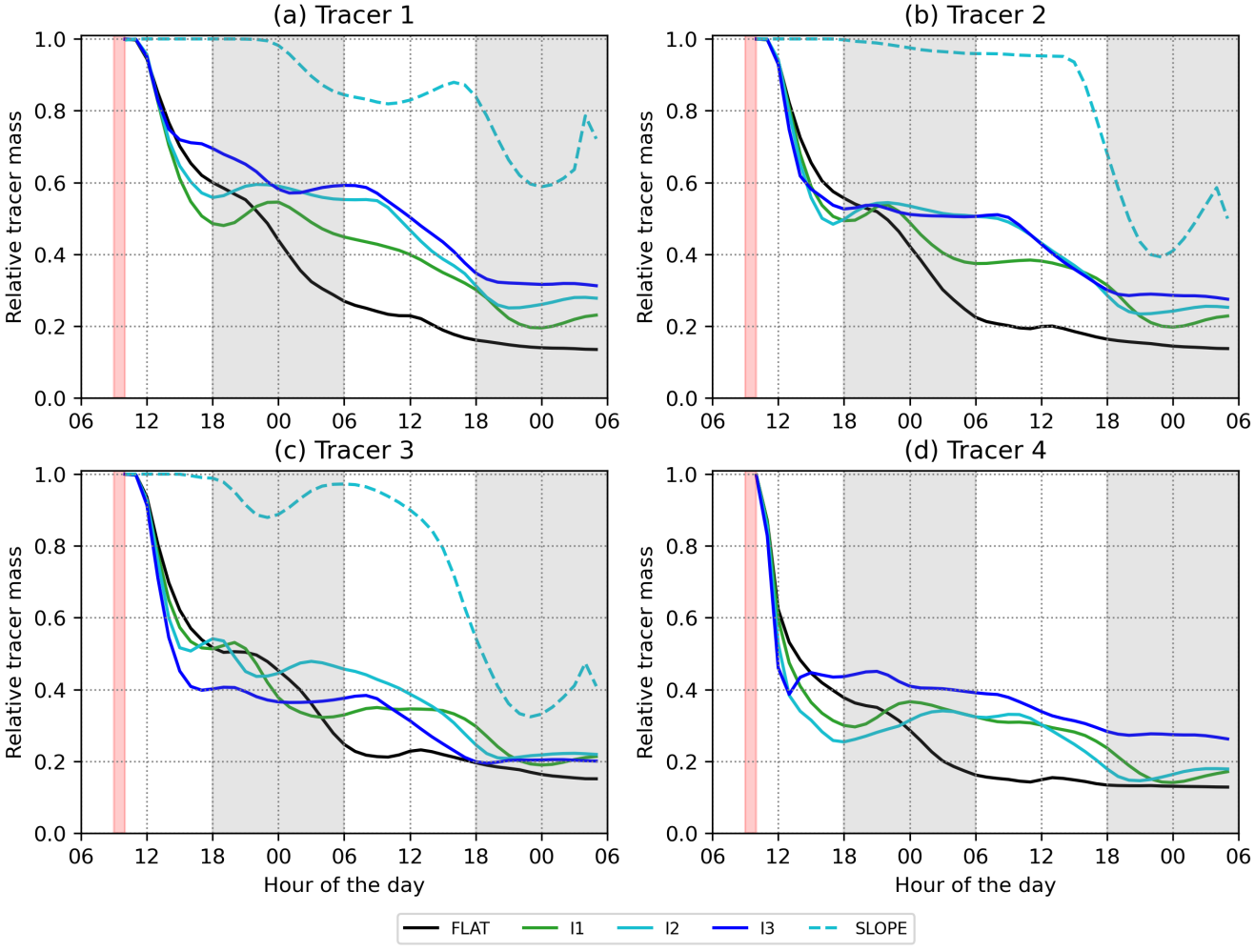

Figure 7. Timeseries of relative tracer mass within the valley volumes. Value 1.0 corresponds to all the released tracer mass being within the valley atmosphere. For the case SLOPE the reference volume is a 2-km layer above the sloped surface. See Fig. 1 for the tracer release locations. Red shaded areas denote the tracer release time and grey shaded areas the timesteps with negative surface sensible heat flux.

center not directly at the valley entrance and its' ventilation out of the valley is distributed the most even between the valley halves (discussed later in this section). Positive values refer to the flux direction shown in Fig. 2, hence positive F1 refers to the horizontal transport of tracer mass from the plain into the valley at the valley entrance and positive F2–F3 refer to the ventilation of tracer mass out of the valley volume normal to the upper lid at the ridge height. The plotted variable, relative tracer flux in the unit of hr^{-1}, for example with a value of 0.1 means that 10% of the tracer mass of that tracer in the whole domain is transported through the corresponding area during that hour.

https://doi.org/10.5194/egusphere-2024-1900
Preprint. Discussion started: 15 July 2024

The aforementioned most intense flux of tracer mass between the valleys and their surroundings during the first six hours after the tracer release occurs at the ridge height (Fig. 8a-d). For the cases FLAT and I3 the vertical flux F2 (i.e. $y < 50$ km) is clearly higher than F3 (i.e. $y > 50$ km) on the first day (Fig. 8a,d). For cases I1 and I2 the ventilation is distributed more evenly between both of the valley halves (Fig. 8b,c). These differences likely stem from the differences in the along-valley extent and strength of the daytime up-valley winds between the cases. In the case FLAT the daytime up-valley winds do not extend far into the upper-half ($y > 50$ km) of the valley, so the ventilation by the cross-valley winds is more concentrated on F2. In the case I3, although the up-valley winds do reach up to the head of the valley, the wind strength is lower which results in weaker along-valley transport of tracer mass compared to the cases I1 and I2.

For tracers 1 (Suppl. Fig. A8) and 4 (Suppl. Fig. A10) F2 is much higher than F3. Tracer 1 is released close to the valley entrance so the tracer mass has more time to ventilate in the lower half of the valley before reaching the top half of the valley. The ventilation of tracer 4 during the first six hours following the release is double in magnitude compared to the other tracers since the tracer 4 is released directly in the cross-valley up-slope circulation so the tracer reach the upper lid of the valley volume shortly after. Ventilation in the upper half of the valley (F3) is dominant for tracer 3 (Suppl. Fig. A9) since this tracer is released at the half-way point of the valley and most of the tracer is transported rapidly into the upper half by the up-valley winds.

Horizontal transport of tracers between the valley volume and the plain occurs at the valley entrance, which is prominent especially during the night in cases FLAT and I1 (negative F1 in Fig. 8a–b). The transport to the plain coincides with the down-valley winds which are also the strongest in cases FLAT and I1. The night-time residual layer up-valley winds and its' associated return flow most likely is the most important for the lateral tracer transport as the surface-based down-valley winds are basically absent in the case FLAT (Section 3.1.3). Cases I2–I3 have weaker night-time down-valley winds occurring in a smaller part of the valley volume hence the outflow of tracer mass during the night is small. Similar behaviour during the night is seen with the other three tracers as well (Suppl. Figures A8–A10).

On the second day the ventilation occurs mostly in the upper-halves of the valleys (Fig. 8a-d). Opposite to the first day, the ventilation from the upper half of the valleys takes place before the lower half. This is likely because on the second day the tracer mass is more spatially distributed in the valleys compared to on the first day when the tracers are much more spatially confined due to their small release areas. The cross-valley circulation does still ventilate the tracer mass located near the valley surface, but the dominant feature appears to be the transport by the along-valley circulation and the lateral boundary induced convergence at the head of the valley. In the inclined valleys, in which the daytime up-valley winds cover the whole length of the valleys, the tracer mass is lifted at the head of the valley (not shown). Some of the lifted tracer is ventilated out of the valley volume and some enters the down-valley directed return flow which is located within the valley volume. In the return flow the tracer mass, transported now down-valley above the CBL_v, encounters the upper half of the valley ridge height before the lower half which is the reason for the ventilation at the upper half taking place before the lower half on the second day.

https://doi.org/10.5194/egusphere-2024-1900
Preprint. Discussion started: 15 July 2024

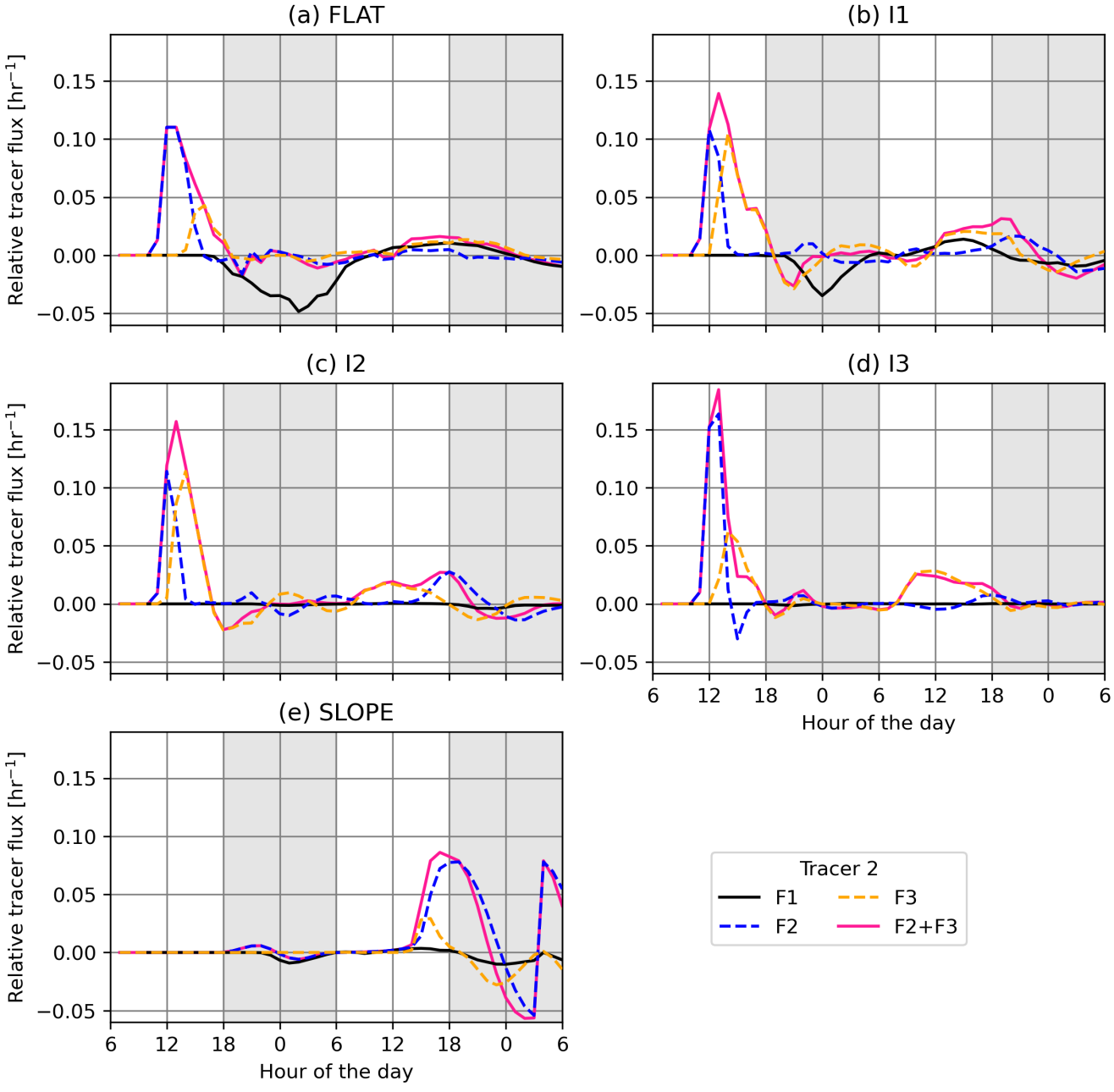

Figure 8. Timeseries of the flux components F1–F3 for Tracer 2. Same Figure but for Tracer 1, 3 and 4 are shown in Suppl. Figures A6–A8. Tracer mass fluxes are normalised by the total tracer mass in the domain (of that tracer in that simulation case). Grey shaded areas the timesteps with negative surface sensible heat flux

https://doi.org/10.5194/egusphere-2024-1900
Preprint. Discussion started: 15 July 2024

The vertical fluxes are clearly weaker in the case SLOPE (Fig. 8e) compared to the valley case I2 (Fig. 8c). In the case SLOPE basically all of the transport of tracers out of the reference volume occurs on the second day around the time the tracer plume reaches the end of the domain and is transported out of the analysis volume by the return flow (not shown). Also on the first day, some of the tracer mass makes it up to the return flow, but the return flow is located below the reference height (discussed in Section 3.1) hence the tracer mass does not leave the analysis volume. The cross-valley circulation is very important for bringing the tracer up to the ridge height in the valley cases, which explains the drastic difference in the fluxes between case I2 and case SLOPE which does not have a cross-valley circulation.

Figure 9 shows the flux components F1–F3 integrated over the whole simulation period for each tracer and case. For tracers 1 and 4 the relative total amount of ventilated tracers (F2+F3) does not depend strongly on the valley inclination (Fig. 9a,d). For tracers 2 and 3 the difference is already large with an increase from 51% (FLAT) to 65% (I3) for tracer 2 (Fig. 9b) and from 49% (FLAT) to 75% (I3) for tracer 3 (Fig. 9c). Whether the ventilation occurs more by F2 or F3 depends heavily on the tracer release location. An important factor in the vertical fluxes is that the ventilation altitude changes between the valleys. Based on the valley topographies, in the case FLAT the ventilation occurs always at 2 km altitude (constant ridge height), for both F2 and F3. In the steepest case I3, the ventilation in F2 occurs between 2 and 4 km and in F3 between 4 and 6 km altitude. This has a significant role in where the ventilated tracers end up in the atmosphere.

The outflow of tracers at the valley entrance decreases with increasing inclination (Fig. 9). This is seen as a decrease in the magnitude of the negative F1 with increasing inclination. This is likely due the weakening night-time down-valley winds and the further penetration of the daytime up-valley winds with the increasing valley inclination (section 3.1.5). Although the surface-based down-valley winds are the weakest for the case FLAT, the elevated return flow in the residual layer is strong especially at the valley entrance. Case FLAT has the strongest night-time outflow of tracers at the valley entrance and the shortest along-valley penetration of the up-valley winds. The up-valley winds do not carry the tracer mass as far into the valley as in the inclined cases I1 and I2. In case I3 the night-time down-valley winds are weak so the night-time horizontal export of tracer mass is seen only for the tracer 1, which is released closest to the valley entrance (Fig. 9a).

https://doi.org/10.5194/egusphere-2024-1900
Preprint. Discussion started: 15 July 2024

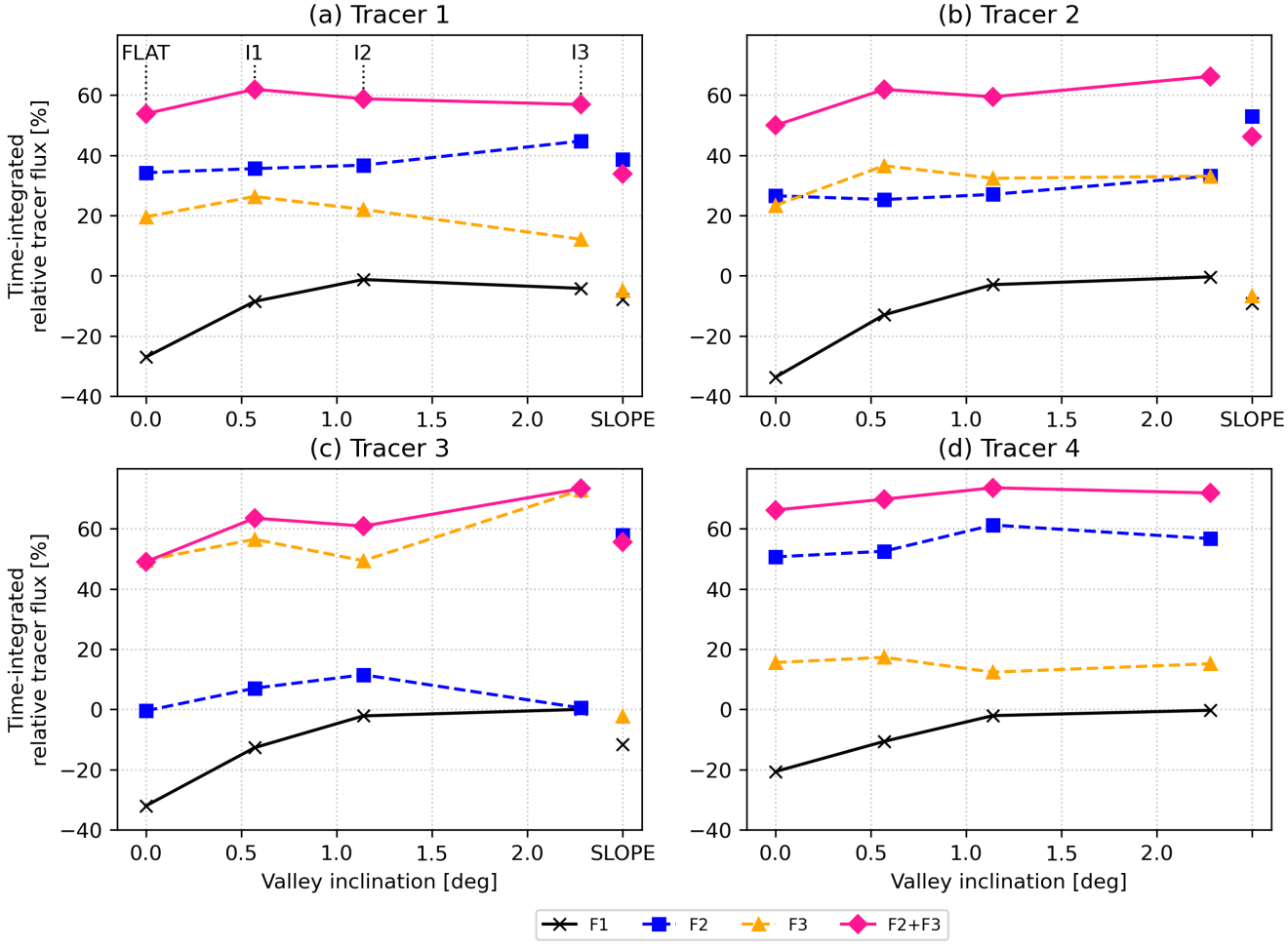

Figure 9. Time integral of the flux components F1–F3 over the whole simulation period for each tracer (a-d) and simulation (valley inclination on the x-axis). Case SLOPE is plotted on the right-hand side of each panel.

3.2.3 Tracer mass distribution in the domain

Figure 10 shows the tracer mass distribution in five sectors during the last hour of the simulations. These sectors are

- 2 km deep surface-based layer above the plain, blue in Fig. 10 ($z \leq 2$ km, $y < 0$ km),
- the valley volume, dark grey ($|x| \leq 10$ km, $y \geq 0$ km, below ridge height),
- the parallel valley, light grey ($|x| > 10$ km, $y \geq 0$ km, below ridge height),
- the rest of the domain above the valley, orange ($y > 0$ km, above ridge height),
- the rest of the domain higher than 2 km above the plain, yellow ($z > 2$ km, $y < 0$ km).

https://doi.org/10.5194/egusphere-2024-1900
Preprint. Discussion started: 15 July 2024

For all tracers, the inclined valleys transport a larger share of the tracer mass to the two highest sectors (orange and yellow) compared to the case FLAT (Fig. 10). Tracers 2 and 3 that are ventilated more from the upper-half of the valley atmosphere result in an increased tracer mass at higher sectors with increasing inclination. Compared to FLAT, in which only about 35% to 40% of the tracers end up far above the surface, between 50% and more than 80% end up there in case of inclined valley floors. Although the fluxes F2 and F3 did not depend strongly on the inclination for tracer 1, the relative tracer mass in the two higher sectors is increased for inclined cases (Fig. 10). This is true also for the tracers that were mostly ventilated in the lower half of the valley in the steepest case I3, since the ridge-height rises up to 4 km by the half-way point of the valley.

For the inclined valleys I1–I3, the tracer mass remaining in the valleys (dark grey shading, Fig. 10) is higher than near the surface above the plain (blue shading). The opposite is found for the FLAT valley, in which the near-surface sector at the plain gathers the most tracer mass. This is explained by the strongest night-time outflow of the tracer mass to the plain at the valley entrance in the case FLAT. The inclined cases accumulate similar amount of tracer mass within the valley volume when compared together. Although more of the tracer mass stays within the valley volume in the inclined valleys, the remaining tracer mass is located at higher altitude compared to the case FLAT (not shown). Hence, the accumulated tracer mass would have the potential to be ventilated at higher altitudes if the simulation was continued further. For example, in case I3 all of the tracer 3 is located above 3 km height at the end of the simulation (not shown). The tracer mass from the plain would also keep ventilating in the case FLAT, but the ventilation occurs always at 2 km height.

The transport of tracer mass out of the analysis volume in SLOPE (2 km deep layer above the sloped surface) is much weaker compared to the valley simulation I2. The amount of tracer mass in the two highest sector volumes (yellow and orange in Fig. 10) is less than what is simulated in I2 and at least 35% up to over 65% of the tracer mass is accumulated in the 2-km deep analysis volume (grey in Fig. 10).

https://doi.org/10.5194/egusphere-2024-1900
Preprint. Discussion started: 15 July 2024

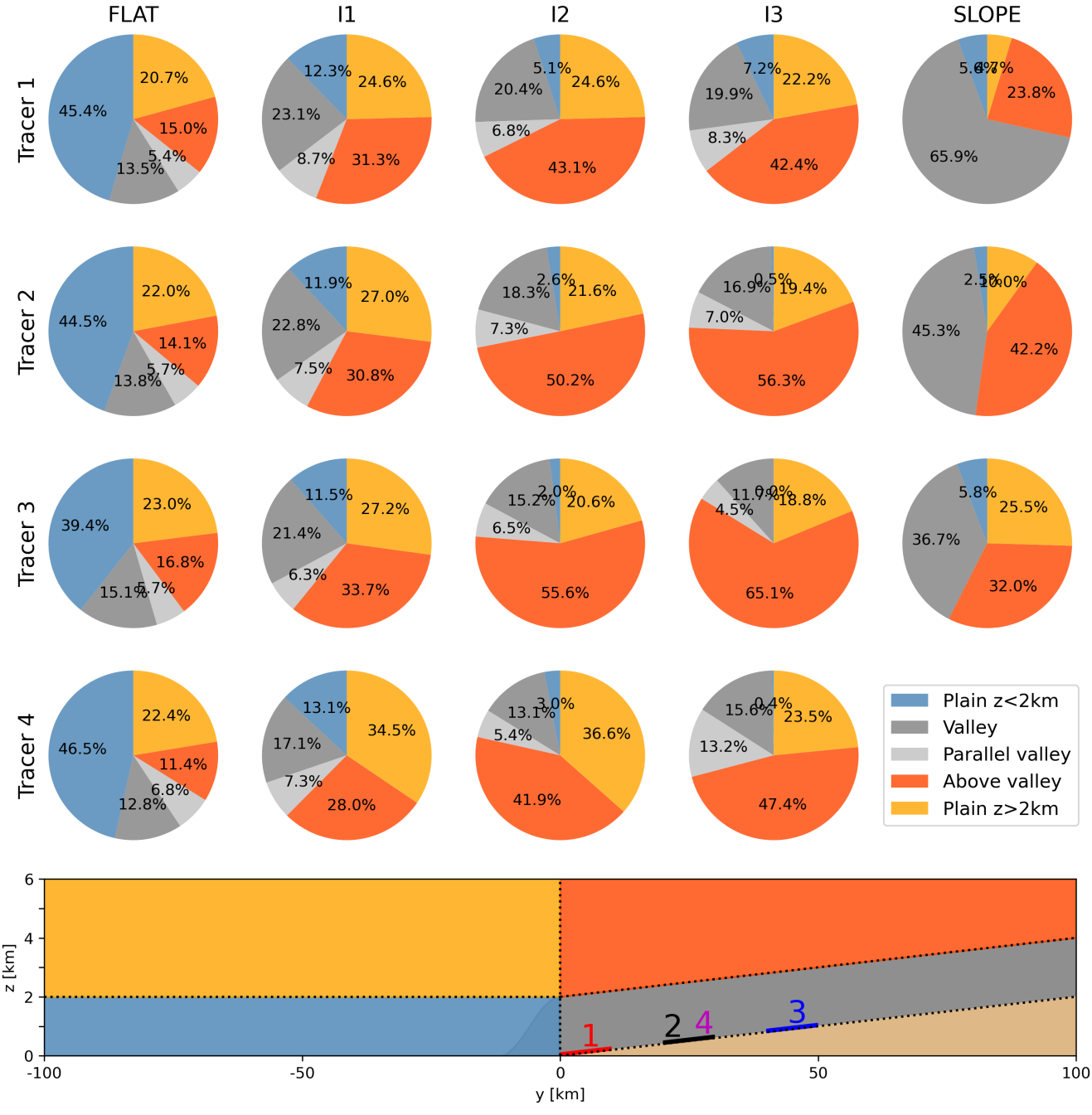

Figure 10. Tracer mass distribution in the shown sectors at the last hour of the simulations. For the valley topographies the sectors *Valley* and *Above valley* are separated by the ridge-height (topography I2 shown). For case SLOPE the Valley and Above valley sectors are separated at 2 km above the surface. Sector *parallel valley* is the remaining part of the domain for the valley simulations at $|x| > 10$ km. Numbers 1-4 in the bottom figure denote the along-valley emission location for the tracers.

https://doi.org/10.5194/egusphere-2024-1900
Preprint. Discussion started: 15 July 2024

4 Discussion

In this section we attempt to explain the differences in the valley winds and tracer transport between the simulated cases. Results of this study are compared to previous publications and new insights of the study are highlighted.

Our study fills the gap between two previous publications, Wagner et al. (2015a) and Mikkola et al. (2023), both of which studied the effects of the valley floor inclination on the daytime up-valley winds. Similarities were found with both studies despite the fact that the valley topographies differed considerably in these two previous studies and consequently they reached opposite conclusions on how the valley floor inclination effects the daytime up-valley winds (introduced in Section 1). Wagner et al. (2015a) found an increase in the valley averaged along-valley wind speed with increased valley floor inclination, which agrees with our simulations when only considering the range of valley inclinations included in their study. The steepest valley floor inclination in Wagner et al. (2015a) is 0.86 degrees which sits between the inclination of the cases I1 (0.57 degrees) and I2 (1.14 degrees) in our idealised experiments. We found the maximum of daytime up-valley wind strength for the case I1 and weaker winds for the steeper cases I2 and I3 (2.28 degrees). Wagner et al. (2015a) found that the daytime up-valley wind maximum was located further into the valleys with inclined valley floors when compared to their flat floor valley. Similarly, in our simulations the case FLAT has a valley entrance jet (Section 3.1) and weak up-valley winds in the interior of the valley. In the inclined cases the up-valley winds are stronger further in the valleys. In order to form prominent up-valley winds far away from the valley entrance, the valley has to exhibit either (local or regional) inhomogeneities such as changing valley cross-valley shape (for example due to narrowing; Wagner et al., 2015a) or an inclination in the valley floor.

The main difference in our idealised topographies to those studied by Wagner et al. (2015a) is the constant cross-sectional area (shape) along the valley. In Wagner et al. (2015a) the ridges have a constant height of 1.5 km, hence the valley floor inclination leads to a reduced valley volume along the valley, which is not the case for our simulations with the constant cross-valley shape throughout the valley. In our case the valley volume is the same in all valley simulations and, thus, also is the topographic amplification factor (TAF) in its traditional form based on the volume ratio. Hence, the traditional TAF does not scale with the strength of the up-valley winds in the inclined valleys of our simulations. The reason for this might be the decreased depth of the up-valley wind layer in the inclined valleys. The up-valley wind layer depth decreases considerably when the valley cross-section reaches above the altitude of CBL_p. For example, in the steepest case I3 on the first day of the simulation this point is reached around the half-way point of the valley (Section 3.1.1). The shallower CBL_v further in the inclined valleys compared to the valley entrance and shallower CBL_v with increasing valley inclination could be explained by Equation 5 in Vergeiner and Dreiseitl (1987). They describe the massflux in up-slope flows, which can be applied to the along-valley winds in our simulations with the inclined valleys. The massflux decreases with increased background stability and inclination. Close to the valley entrance the background stability for the anabatic up-valley winds is the near-neutral CBL_p where as further up in the valley located above the altitude of CBL_p the background environment is the stably stratified atmosphere. Comparison within the inclined valleys is rather simple; steeper valley inclination yields decreased along-valley massflux (Vergeiner and Dreiseitl, 1987) hence shallower and weaker up-valley winds in our case. Further in the inclined valleys where the CBL_v is shallower, the portion of cross-valley up-slope winds flowing outside of the CBL_v increase. This also means a larger share of

https://doi.org/10.5194/egusphere-2024-1900
Preprint. Discussion started: 15 July 2024

the heat provided from the valley surface is likely not driving the up-valley winds by the valley volume effect. This would also explain why TAF does not scale with the up-valley wind speeds within the inclined valleys, as the TAF argument is based on negligible heat export out of the valley volume. In this way the steep valley inclination likely shifts the driving mechanism of the up-valley winds from the valley volume effect to the buoyancy forcing, instead of combining these two. Far in the valley, above the altitude of CBL_p, the up-valley winds resemble anabatic winds driven by the buoyancy forcing due to the heated sloped surface.

Our steepest valley case I3 has approximately the same inclination in the valley floor and ridges as the steeply inclined (2–5 degrees) Himalayan valleys studied in Mikkola et al. (2023). Our finding of decreasing up-valley wind strength and depth with increasing valley inclination supports the findings of Mikkola et al. (2023). The valley inclinations in Mikkola et al. (2023) are much steeper than considered in Wagner et al. (2015a), which caused the conflict in the results of these two studies. In the steep Himalayan valleys above the altitude of the CBL_p, the up-valley winds flow in a shallow layer, which is seen also in our simulations.

The optimal angle for strengthening the up-valley winds is probably determined by the valley geometry, CBL_p depth and the background stability. The valley ridge height, inclination and the CBL_p depth would determine how large a share of the valley volume is characterised by (1) the shallower anabatic up-valley winds flowing above the CBL_p or (2) the anabatic up-valley winds flowing below the CBL_p acting together with the valley volume effect driven up-valley winds with enhancing impact. Valley inclination and the stability of the atmosphere above the up-valley wind layer would influence the buoyant forcing of the along-valley winds affecting the strength and depth of the anabatic up-valley winds.

The inclined valleys were found to have daytime vertically stacked circulation in along-valley direction (Section 3.1.1). Such stacked circulation cells have previously been found only in the cross-valley circulation but in the along-valley direction this type of stacked circulation has not been documented in previous publications. The weak secondary cell above the main valley circulation is likely being dominated easily by the background flow or pressure gradients which do not exist in our simulations. This would explain the lack of published observational or modelling studies referring to this flow feature in real valleys. Authors are not aware of previous idealised studies with similar inclined valley topographies which is suggested being the crucial topographic feature for forming this stacked circulation in along-valley direction.

Similar to the passive tracers in our simulations the parcels from the valley entrance were transported faster into the valley with inclined valley floor in Wagner et al. (2015a) when compared to the flat floor valley. This occurs due to the higher wind speeds in the inclined valleys (Wagner et al., 2015a) but also probably due the further along-valley spread of the up-valley winds. Also in their simulations the transport out of the valley occurs closer to the valley entrance for the flat floor valley, similar to our case FLAT. Also the transport to the plain by the return flow was weaker for the valley with inclined valley floor. This is probably due the further transport of the tracers during daytime and weaker down-valley winds during the night. In the case of Wagner et al. (2015a) the ventilation occurred at the same height for each of the valley so the valley floor inclination did not change the final height distribution of the tracer mass as it did in our simulations. In our case, the tracer ventilation occurs at higher altitudes with increasing inclination. The tracers are transported by the up-valley winds before they exit the

https://doi.org/10.5194/egusphere-2024-1900
Preprint. Discussion started: 15 July 2024

valley volume at the upper lid of the valley volume, which means that the tracer mass is lifted in vertical prior the ventilation and the ventilation occurs at higher altitude.

Although the along-slope winds in the case SLOPE were not that different to the along-valley winds in the case I2 with the same inclination, the transport of tracers differs a lot. Transport of tracers out from the 2 km deep layer above the sloped surface was much weaker than the transport out of the valley volume in case I2. The cross-valley circulation bringing the tracer to the ridge-height is crucial in the ventilation, rather than the along-valley winds that have more or less similar magnitude as the along-slope winds in the case SLOPE. This highlights the importance of the vertical transport by mean cross-valley circulation for accurate representation of the mountain ventilation that needs to be either resolved or parameterized. Coarse resolution could resolve the mean winds and the along-valley transport with decent accuracy when considering only the inclination but the transport processes are not simulated properly without resolving the cross-valley circulation in the valley.

Bianchi et al. (2021) suggested the valleys at the southern slope of the Himalayan mountain range acting as sources of free-tropospheric aerosol. The daytime up-valley winds were proposed bringing the aerosol up to the high elevation of 5 km within the valley volume before the ventilation takes place. Wind comparison of four Himalayan valleys in Mikkola et al. (2023) supported this hypothesis as the other valleys had also up-valley winds reaching to these high altitudes within the valleys. Our simulations show the inclined valleys, alike the Himalayan valleys studied by Bianchi et al. (2021) and Mikkola et al. (2023), to be efficient in transporting tracer mass from the low elevations of the valleys up to high elevations in the free troposphere. In our simulations the steepest valley ventilated the tracers to the highest in the atmosphere (Section 3.2.3). Ventilation to the high elevations favors long-range transport and longer lifetime for the aerosol hence higher potential for climate impact in the free troposphere.

So far, we have investigated the impact of valley inclination with only one combination of the surface sensible heat flux and initial temperature profile. Different combinations of the surface heating, valley inclination and initial stability could reveal more details on which features are the most important in determining the optimal angle for strengthening the daytime up-valley winds. The lateral boundary conditions in along-valley direction define how the up-valley flow behaves at the head of the valleys. This is especially prominent in the inclined valleys which show well defined up-valley winds for whole length of the valleys and develop strong return flow at the head of the valley due the forced convergence near the domain boundary. This resembles a mountain ridge where an identical valley would oppose at the head of the valley (not taking to account the effects of the south/north orientation on the thermally-driven winds). Larger domain with a plateau following the head of the valley would resemble better the Himalayan valleys studied in Mikkola et al. (2023) and could give interesting insights for the transport of the tracers into the free troposphere but also through the valley. These Himalayan valleys open up to the Tibetan plateau at the head of the valleys and in the idealised simulations this would allow lateral transport through the valley in addition to the lateral transport at the valley entrance and vertical transport at the upper lid of the valley. However, this would substantially increase the computational requirements of the simulations. The night-time surface-based down-valley winds are likely sensible for the surface cooling, which is in our simulations a constant -10 W m^{-2}. With stronger night-time cooling, the surface-based down-valley wind layer could grow in height, making the residual layer up-valley winds less dominant feature.

https://doi.org/10.5194/egusphere-2024-1900
Preprint. Discussion started: 15 July 2024

5 Conclusions

We study the effects of valley inclination on the valley winds and transport of passive tracers using high-resolution WRF-simulations. Four idealised valley topographies with differing valley inclination and one experiment with a flat slope were simulated. Focus of the analysis is on the along-valley winds and transport of passive tracers out of the valley volume. The key findings are as follows.

- The valley inclination allow daytime up-valley winds to penetrate further into the valley, compared to flat-floored valleys where strong winds are limited to the entrance. Additionally, steeper inclinations strengthen daytime up-valley winds, but only up to a certain point. Beyond that critical angle, the winds weaken again.
- The flat floored valley has the strongest average night-time down-valley winds, although the surface-based down-valley winds are prominent only in the inclined valleys. The night-time residual layer within the valley volume is characterised with up-valley winds and return flow, which weaken with increasing valley inclination.
- Steeper valleys allow daytime winds to carry passive tracers deeper into the valley before they are ventilated out of the valley. Consequently, this ventilation occurs in steeper valleys at a higher altitude than for the flat-floored valley.
- The flat-floored valley exhibits stronger overall tracer outflow compared to inclined valleys. However, this higher outflow occurs at lower altitude due to the lower crest height. This confines the majority of the ventilated tracers to the lowest few kilometers of the atmosphere. Therefore, steep valleys are more efficient in ventilating tracers to the upper troposphere, where long-range transport can take place.

Increased number of experiments with differing valley shape, initial profile of temperature and surface heating could give more insights on the controlling factors which define the optimal angle of strengthening the daytime up-valley winds. Future studies could incorporate physical and chemical modelling of aerosol processes, instead of the passive tracers, with the idealised valley setup. The coupled effects of aerosol population within the valley atmosphere and the valley winds hence the transport of aerosol could be studied using the idealised valley topographies. Realistic surface emission, aerosol removal and production processes could reveal insights what happens to the aerosol prior the ventilation out of the valley.

https://doi.org/10.5194/egusphere-2024-1900
Preprint. Discussion started: 15 July 2024

Appendix A: Averaged air mass transport

This is a step-by-step derivation for the along-valley averaged air mass transport, plotted in Fig. 6 and discussed in Section 3.1.5. First, we start with along-valley directed horizontal dry air mass flux, $v(t,x,y,z) \cdot \rho_d(t,x,y,z)$, which has the unit of m s $^{-1}$ kg m $^{-3}$. v is the y-component of the wind and ρ_d is the dry air density. Next we integrate the dry air mass flux over each valley cross-section in x-z plain, which we mark by $A(t,y)$:

$$A(t,y) = \int_{x=-10\text{km}}^{x=10\text{km}} \int_{z=0}^{z(y)=\text{ridge height}} v(t,x,y,z) \cdot \rho_d(t,x,y,z) dz dx$$

, which has the unit of kg s $^{-1}$. Now we take spatial average in along-valley direction, which results as one value of averaged integrated mass flux in y-direction for each timestep, which is marked by $B(t)$:

$$B(t) = \frac{1}{L_y} \int_{y_i=0}^{L_y} A(t,y_i)$$

, where L_y is the length of the valley. Finally, we integrate over the selected time period

$$\int_t B(t) dt$$

and end up with the along-valley averaged air mass transport, which has the unit of kg.

Code and data availability. The WRF model code and analysis scripts are available in Zenodo (Mikkola, 2024b). The hourly averaged WRFlux output of the variables needed to reproduce the figures in this article are available in IDA fairdata database (Mikkola, 2024a). The instantaneous WRF output is available upon request (contact author).

Author contributions. JM did the WRF simulations with the help of AG and VAS. JM performed the data analysis with the help of AG, VAS and FB. JM wrote most of the manuscript with input from AG and VAS. All authors contributed on planning the research and discussed the final form of the manuscript.

Competing interests. The contact author has declared that none of the authors has any competing interests.

Acknowledgements. This research has been supported by the H2020 European Research Council (grant no. 850614) and the Vilho, Yrjö and Kalle Väisälä Foundation of the Finnish Academy of Science and Letters.

https://doi.org/10.5194/egusphere-2024-1900
Preprint. Discussion started: 15 July 2024

References

Bianchi, F., Junninen, H., Bigi, A., Sinclair, V., Dada, L., Hoyle, C., Zha, Q., Yao, L., Ahonen, L., Bonasoni, P., Buenrostro Mazon, S., Hutterli, M., Laj, P., Lehtipalo, K., Kangasluoma, J., Kerminen, V., Kontkanen, J., Marinoni, A., Mirme, S., Molteni, U., Petaja, T., Riva, M., Rose, C., Sellegri, K., Yan, C., Worsnop, D., Kulmala, M., Baltensperger, U., and Dommen, J.: "Biogenic particles formed in the Himalaya as an important source of free tropospheric aerosols", Nature Geoscience, 14, 4–9, https://doi.org/10.1038/s41561-020-00661-5, 2021.

Bollasina, M., Bertolani, L., and Tartari, G.: Meteorological observations at high altitude in the Khumbu Valley, Nepal Himalayas, 1994-1999, Bull. Glaciol. Res., 19, 1–11, 2002.

Bonasoni, P., Laj, P., Marinoni, A., Sprenger, M., Angelini, F., Arduini, J., Bonafè, U., Calzolari, F., Colombo, T., Decesari, S., Di Biagio, C., di Sarra, A. G., Evangelisti, F., Duchi, R., Facchini, M., Fuzzi, S., Gobbi, G. P., Maione, M., Panday, A., Roccato, F., Sellegri, K., Venzac, H., Verza, G., Villani, P., Vuillermoz, E., and Cristofanelli, P.: Atmospheric Brown Clouds in the Himalayas: first two years of continuous observations at the Nepal Climate Observatory-Pyramid (5079 m), Atmospheric Chemistry and Physics, 10, 7515–7531, https://doi.org/10.5194/acp-10-7515-2010, 2010.

Farina, S. and Zardi, D.: Understanding Thermally Driven Slope Winds: Recent Advances and Open Questions, Boundary-Layer Meteorology, 189, 5–52, https://doi.org/10.1007/s10546-023-00821-1, 2023.

Gohm, A., Harnisch, F., Vergeiner, J., Obleitner, F., Schnitzhofer, R., Hansel, A., Fix, A., Neininger, B., Emeis, S., and Schaefer, K.: Air Pollution Transport in an Alpine Valley: Results From Airborne and Ground-Based Observations, Boundary-Layer Meteorology, 131, https://doi.org/10.1007/s10546-009-9371-9, 2009.

Gordon, H., Kirkby, J., Baltensperger, U., Bianchi, F., Breitenlechner, M., Curtius, J., Dias, A., Dommen, J., Donahue, N. M., Dunne, E. M., Duplissy, J., Ehrhart, S., Flagan, R. C., Frege, C., Fuchs, C., Hansel, A., Hoyle, C. R., Kulmala, M., Kürten, A., Lehtipalo, K., Makhmutov, V., Molteni, U., Rissanen, M. P., Stozkhov, Y., Tröstl, J., Tsagkogeorgas, G., Wagner, R., Williamson, C., Wimmer, D., Winkler, P. M., Yan, C., and Carslaw, K. S.: Causes and importance of new particle formation in the present-day and preindustrial atmospheres, Journal of Geophysical Research: Atmospheres, 122, 8739–8760, https://doi.org/https://doi.org/10.1002/2017JD026844, 2017.

Göbel, M.: WRFlux v.1.4.1 Github repository, https://github.com/matzegoebel/WRFlux/releases/tag/v1.4.1, 2022.

Göbel, M., Serafin, S., and Rotach, M. W.: Numerically consistent budgets of potential temperature, momentum, and moisture in Cartesian coordinates: application to the WRF model, Geoscientific Model Development, 15, 669–681, https://doi.org/10.5194/gmd-15-669-2022, 2022.

Göbel, M., Serafin, S., and Rotach, M. W.: Adverse impact of terrain steepness on thermally driven initiation of orographic convection, Weather and Climate Dynamics, 4, 725–745, https://doi.org/10.5194/wcd-4-725-2023, 2023.

Henne, S., Furger, M., Nyeki, S., Steinbacher, M., Neininger, B., de Wekker, S. F. J., Dommen, J., Spichtinger, N., Stohl, A., and Prévôt, A. S. H.: Quantification of topographic venting of boundary layer air to the free troposphere, Atmospheric Chemistry and Physics, 4, 497–509, https://doi.org/10.5194/acp-4-497-2004, 2004.

Hersbach, H., Bell, B., Berrisford, P., Hirahara, S., Horányi, A., Muñoz-Sabater, J., Nicolas, J., Peubey, C., Radu, R., Schepers, D., Simmons, A., Soci, C., Abdalla, S., Abellan, X., Balsamo, G., Bechtold, P., Biavati, G., Bidlot, J., Bonavita, M., De Chiara, G., Dahlgren, P., Dee, D., Diamantakis, M., Dragani, R., Flemming, J., Forbes, R., Fuentes, M., Geer, A., Haimberger, L., Healy, S., Hogan, R. J., Hólm, E., Janisková, M., Keeley, S., Laloyaux, P., Lopez, P., Lupu, C., Radnoti, G., de Rosnay, P., Rozum, I., Vamborg, F., Vil-

https://doi.org/10.5194/egusphere-2024-1900
Preprint. Discussion started: 15 July 2024

laume, S., and Thépaut, J.-N.: The ERA5 global reanalysis, Quarterly Journal of the Royal Meteorological Society, 146, 1999–2049, https://doi.org/https://doi.org/10.1002/qj.3803, 2020.

Hindman, E. E. and Upadhyay, B. P.: Air pollution transport in the Himalayas of Nepal and Tibet during the 1995–1996 dry season, Atmospheric Environment, 36, 727–739, https://doi.org/https://doi.org/10.1016/S1352-2310(01)00495-2, 2002.

Hong, S. and Lim, J.-O. J.: The WRF Single-Moment 6-Class Microphysics Scheme (WSM6), Asia-pacific Journal of Atmospheric Sciences, 42, 129–151, 2006.

Jiménez, P. A., Dudhia, J., González-Rouco, J. F., Navarro, J., Montávez, J. P., and García-Bustamante, E.: A Revised Scheme for the WRF Surface Layer Formulation, Monthly Weather Review, 140, 898 – 918, https://doi.org/https://doi.org/10.1175/MWR-D-11-00056.1, 2012.

Lang, M. N., Gohm, A., and Wagner, J. S.: The impact of embedded valleys on daytime pollution transport over a mountain range, Atmospheric Chemistry and Physics, 15, 11 981–11 998, https://doi.org/10.5194/acp-15-11981-2015, 2015.

Leukauf, D., Gohm, A., and Rotach, M. W.: Toward Generalizing the Impact of Surface Heating, Stratification, and Terrain Geometry on the Daytime Heat Export from an Idealized Valley, Journal of Applied Meteorology and Climatology, 56, 2711 – 2727, https://doi.org/10.1175/JAMC-D-16-0378.1, 2017.

Li, J.-G. and Atkinson, B. W.: Transition Regimes in Valley Airflows, Boundary-Layer Meteorology, 91, 385–411, https://doi.org/10.1023/A:1001846005338, 1999.

Mikkola, J.: Data for "Valley floor inclination affecting valley winds and transport of passive tracers in idealised simulations", https://doi.org/10.23729/234cb096-eec7-4f9b-b37b-435228df3996, University of Helsinki, 2024a.

Mikkola, J.: Model and analysis code for "Valley floor inclination affecting valley winds and transport of passive tracers in idealised simulations", https://doi.org/10.5281/zenodo.12178614, Zenodo, 2024b.

Mikkola, J., Sinclair, V. A., Bister, M., and Bianchi, F.: Daytime along-valley winds in the Himalayas as simulated by the Weather Research and Forecasting (WRF) model, Atmospheric Chemistry and Physics, 23, 821–842, https://doi.org/10.5194/acp-23-821-2023, 2023.

Rotach, M. W., Wohlfahrt, G., Hansel, A., Reif, M., Wagner, J., and Gohm, A.: The World is Not Flat: Implications for the Global Carbon Balance, Bulletin of the American Meteorological Society, 95, 1021 – 1028, https://doi.org/10.1175/BAMS-D-13-00109.1, 2014.

Schmidli, J.: Daytime Heat Transfer Processes over Mountainous Terrain, Journal of the Atmospheric Sciences, 70, 4041 – 4066, https://doi.org/10.1175/JAS-D-13-083.1, 2013.

Schmidli, J. and Rotunno, R.: Mechanisms of Along-Valley Winds and Heat Exchange over Mountainous Terrain, Journal of the Atmospheric Sciences, 67, 3033 – 3047, https://doi.org/10.1175/2010JAS3473.1, 2010.

Schmidli, J. and Rotunno, R.: The Quasi-Steady State of the Valley Wind System, Frontiers in Earth Science, 3, https://doi.org/10.3389/feart.2015.00079, 2015.

Schumann, U.: Large-eddy simulation of the up-slope boundary layer, Quarterly Journal of the Royal Meteorological Society, 116, 637–670, https://doi.org/https://doi.org/10.1002/qj.49711649307, 1990.

Serafin, S., Adler, B., Cuxart, J., De Wekker, S., Gohm, A., Grisogono, B., Kalthoff, N., Kirshbaum, D., Rotach, M., Schmidli, J., Stiperski, I., Vecenaj, Z., and Zardi, D.: Exchange Processes in the Atmospheric Boundary Layer Over Mountainous Terrain, Atmosphere, 9, 102, https://doi.org/10.3390/atmos9030102, 2018.

Skamarock, C., Klemp, B., Dudhia, J., Gill, O., Liu, Z., Berner, J., Wang, W., Powers, G., Duda, G., Barker, D. M., and Huang, X.: A Description of the Advanced Research WRF Model Version 4, 2019.

https://doi.org/10.5194/egusphere-2024-1900
Preprint. Discussion started: 15 July 2024

Venzac, H., Sellegri, K., Laj, P., Villani, P., Bonasoni, P., Marinoni, A., Cristofanelli, P., Calzolari, F., Fuzzi, S., Decesari, S., Facchini, M.-C., Vuillermoz, E., and Verza, G. P.: High frequency new particle formation in the Himalayas, Proceedings of the National Academy of Sciences of the United States of America, 105, 15 666–15 671, https://doi.org/10.1073/pnas.0801355105, 2008.

Vergeiner, I. and Dreiseitl, E.: Valley winds and slope winds — Observations and elementary thoughts, Meteorology and Atmospheric Physics, 36, 264–286, https://doi.org/10.1007/BF01045154, 1987.

Wagner, A.: Theorie und Beobachtung der periodischen Gebirgswinde (Theory and observation of periodic mountain winds)., Gerl. Beitr. Geophys, 52, 408–449, "[English translation: Whiteman, C. D., and E. Dreiseitl, 1984: Alpine Meteorology: Translations of Classic Contributions by A. Wagner, E. Ekhart and F. Defant, PNL-5141/ASCOT-84-3, Pacific Northwest Laboratory, 11–43.]", 1938.

Wagner, J., Gohm, A., and Rotach, M.: Influence of along-valley terrain heterogeneity on exchange processes over idealized valleys, Atmospheric Chemistry and Physics, 15, https://doi.org/10.5194/acp-15-6589-2015, 2015a.

Wagner, J. S., Gohm, A., and Rotach, M. W.: The Impact of Horizontal Model Grid Resolution on the Boundary Layer Structure over an Idealized Valley, Monthly Weather Review, 142, 3446 – 3465, https://doi.org/10.1175/MWR-D-14-00002.1, 2014.

Wagner, J. S., Gohm, A., and Rotach, M. W.: The impact of valley geometry on daytime thermally driven flows and vertical transport processes, Quarterly Journal of the Royal Meteorological Society, 141, 1780–1794, https://doi.org/10.1002/qj.2481, 2015b.

Weigel, A., Chow, F., Rotach, M., Street, R., and Xue, M.: High-Resolution Large-Eddy Simulations of Flow in a Steep Alpine Valley. Part II: Flow Structure and Heat Budgets, J. Appl. Meteorol. Climatol., 45, https://doi.org/10.1175/JAM2323.1, 2006.

Whiteman, C.: Mountain Meteorology: Fundamentals and Applications, https://doi.org/10.1093/oso/9780195132717.001.0001, 2000.

Whiteman, C. D. and Doran, J. C.: The Relationship between Overlying Synoptic-Scale Flows and Winds within a Valley, Journal of Applied Meteorology and Climatology, 32, 1669 – 1682, https://doi.org/10.1175/1520-0450(1993)032<1669:TRBOSS>2.0.CO;2, 1993.

Whiteman, C. D. and Dreiseitl, E.: Alpine meteorology: translations of classic contributions by A. Wagner, E. Ekhart, and F. Defant, https://doi.org/10.2172/6665518, 1984.

Whiteman, C. D., Hoch, S. W., Horel, J. D., and Charland, A.: Relationship between particulate air pollution and meteorological variables in Utah's Salt Lake Valley, Atmospheric Environment, 94, 742–753, https://doi.org/https://doi.org/10.1016/j.atmosenv.2014.06.012, 2014.

Yu, Y., Cai, X., King, J. C., and Renfrew, I. A.: Numerical simulations of katabatic jumps in Coats Land, Antarctica, Boundary-Layer Meteorology, 114, 413–437, https://doi.org/10.1007/s10546-004-9564-1, 2005.

Zängl, G., Egger, J., and Wirth, V.: Diurnal Winds in the Himalayan Kali Gandaki Valley. Part II: Modeling, Monthly Weather Review, "129", "1062 – 1080", https://doi.org/"10.1175/1520-0493(2001)129<1062:DWITHK>2.0.CO;2", 2001.

Zardi, D. and Whiteman, C. D.: Diurnal Mountain Wind Systems, Springer Netherlands, https://doi.org/10.1007/978-94-007-4098-3_2, 2013.

https://doi.org/10.5194/egusphere-2024-1900
Preprint. Discussion started: 15 July 2024

Table A1. Tracer release locations and times in cases FLAT, I1, I2 and I3

Tracer	y-release	x-release	Release start	Release duration
1	0 ... 10 km	-2 ... 2 km	Day 1 09:00am	60 min
2	20 ... 30 km	-2 ... 2 km	Day 1 09:00am	60 min
3	40 ... 50 km	-2 ... 2 km	Day 1 09:00am	60 min
4	20 ... 30 km	2 ... 6 km	Day 1 09:00am	60 min

Table A2. Tracer release locations and times in case SLOPE

Tracer	y-release	x-release	Release start	Release duration
1	0 ... 10 km	-20 ... 20 km	Day 1 09:00am	60 min
2	20 ... 30 km	-20 ... 20 km	Day 1 09:00am	60 min
3	40 ... 50 km	-20 ... 20 km	Day 1 09:00am	60 min

https://doi.org/10.5194/egusphere-2024-1900
Preprint. Discussion started: 15 July 2024

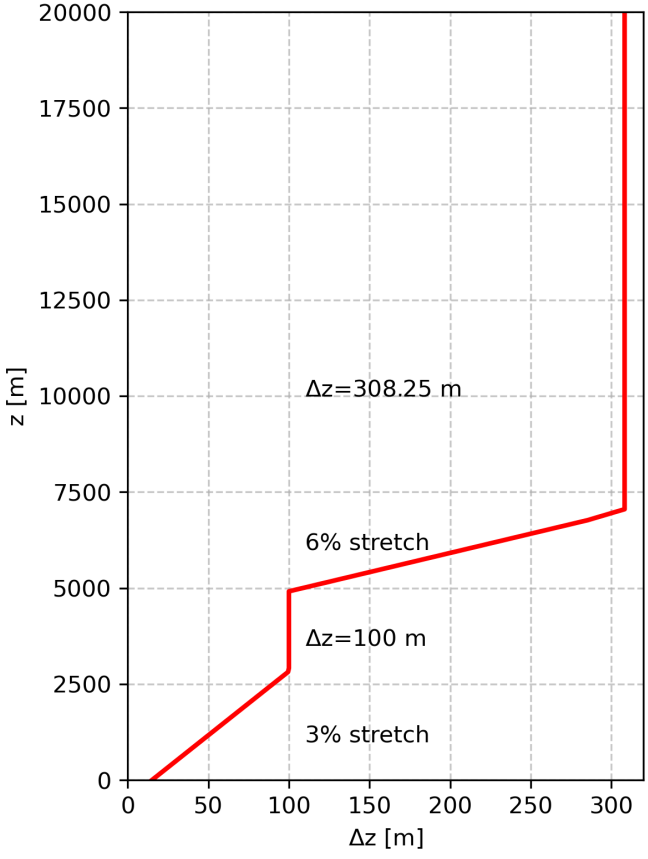

Figure A1. Vertical spacing of the model levels in the simulations (shown for grid points with surface height at 0 meters).

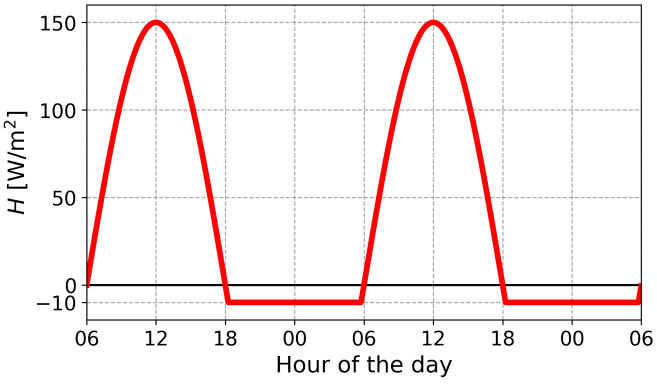

Figure A2. Prescribed surface sensible heat flux in the simulations (Eq. 1 in Section 2).

https://doi.org/10.5194/egusphere-2024-1900
Preprint. Discussion started: 15 July 2024

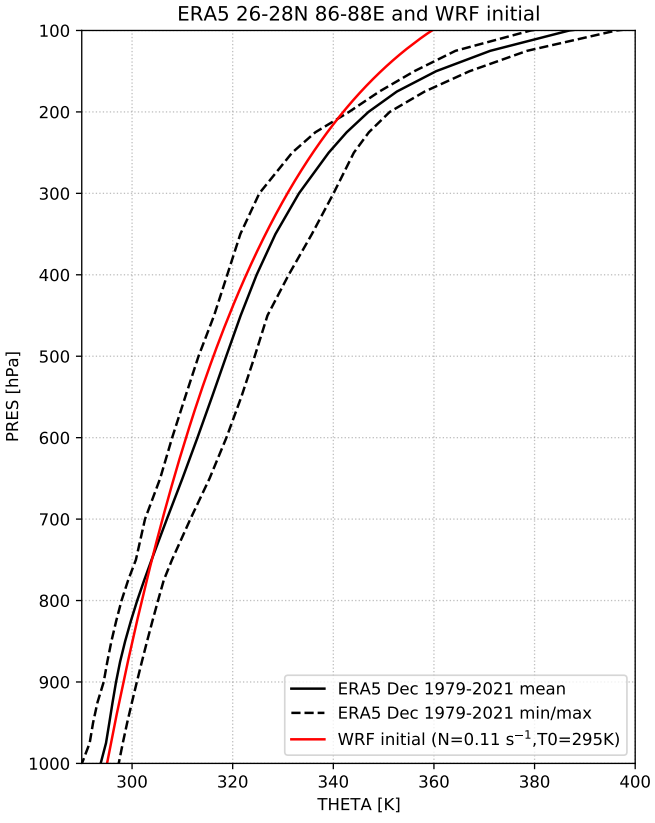

Figure A3. Initial temperature profile of the WRF-simulations and ERA5 1979-2021 December average profile for 26-28N 86-88E.

https://doi.org/10.5194/egusphere-2024-1900
Preprint. Discussion started: 15 July 2024

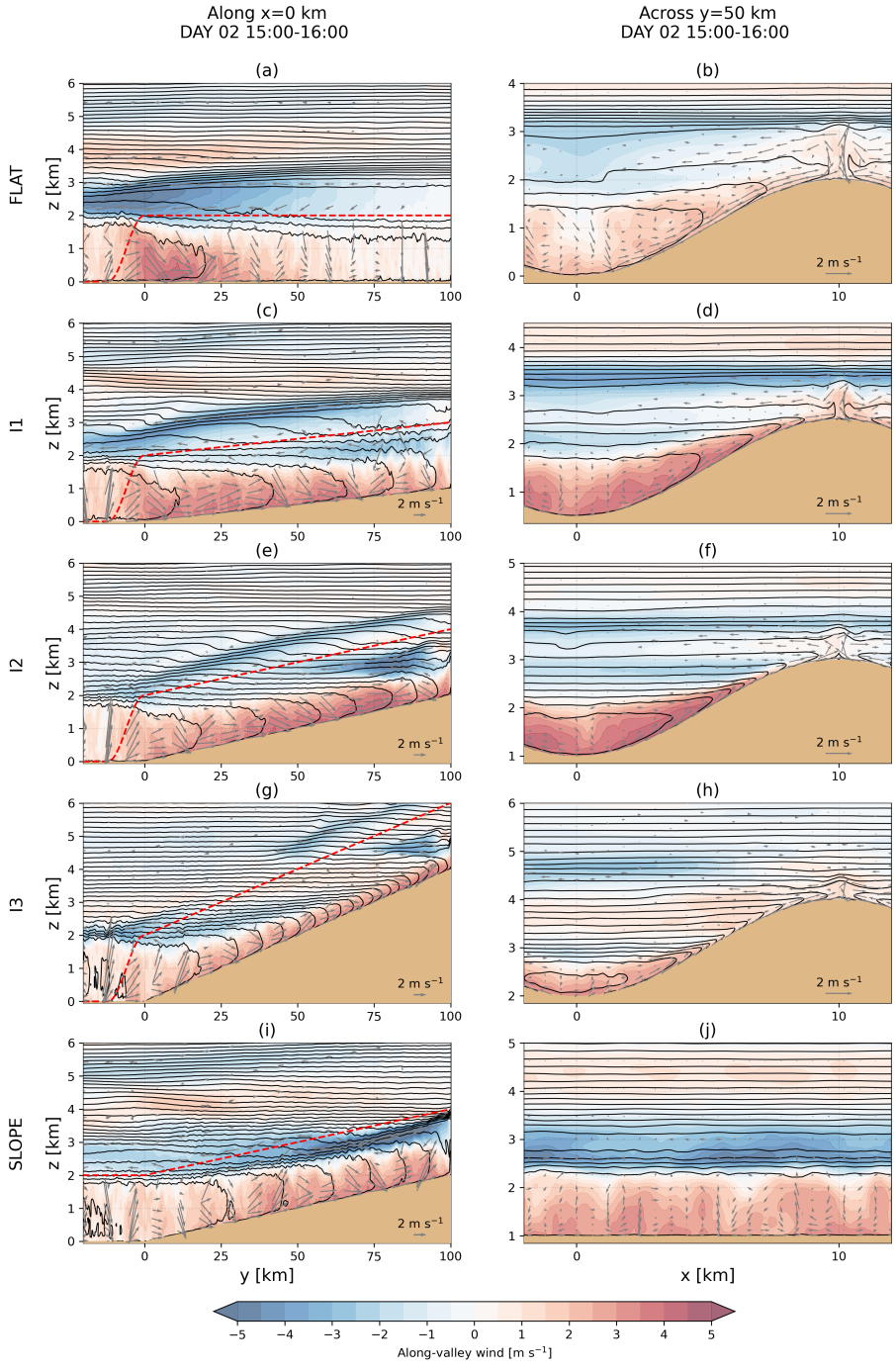

Figure A4. Same as Fig. 3 in the main text but for the second day of the simulation at 15:00-16:00.

https://doi.org/10.5194/egusphere-2024-1900
Preprint. Discussion started: 15 July 2024

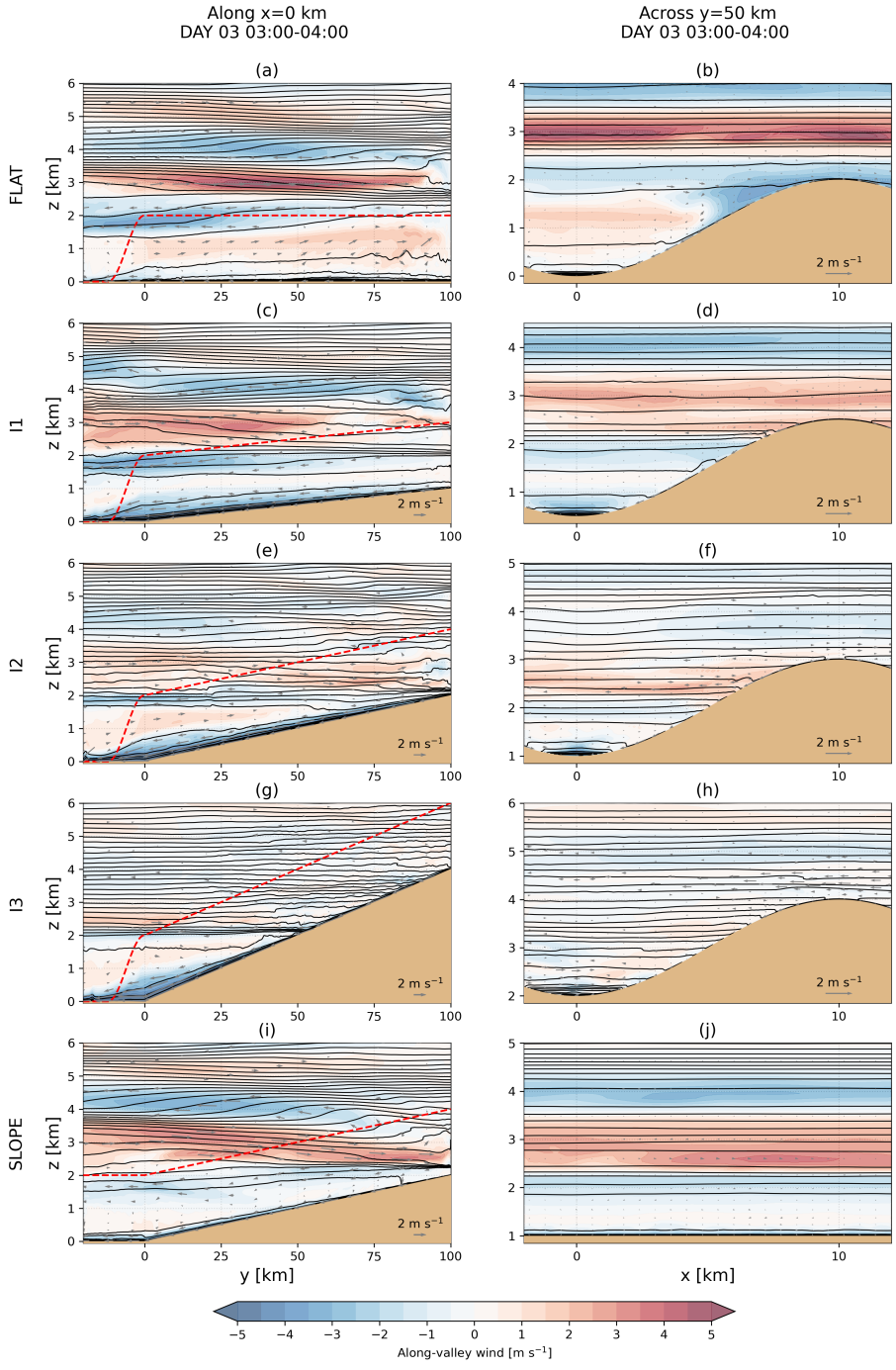

Figure A5. Same as Fig. 4 in the main text but for the second night of the simulation at 03:00-04:00.

https://doi.org/10.5194/egusphere-2024-1900
Preprint. Discussion started: 15 July 2024

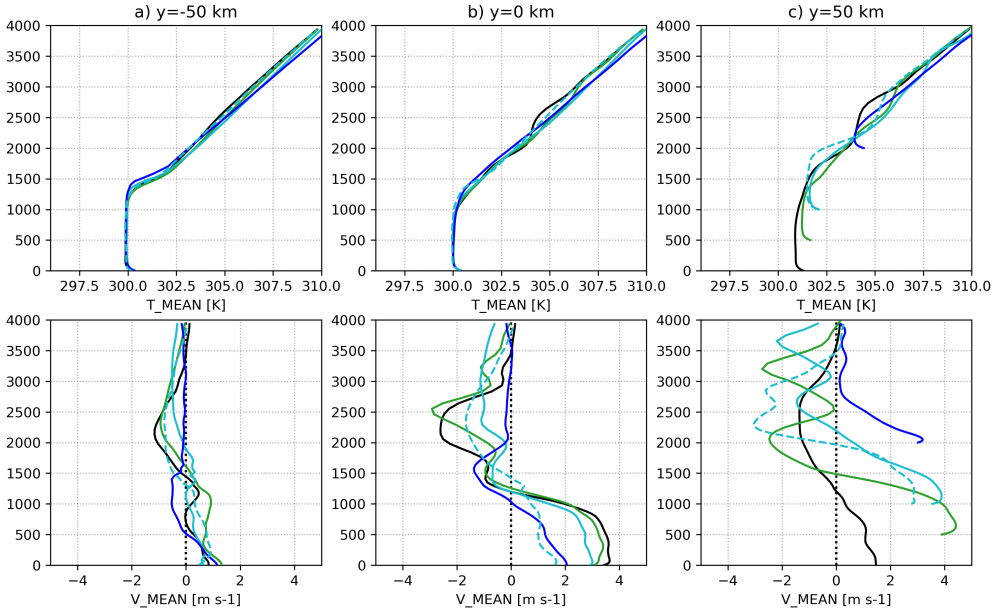

Figure A6. Potential temperature (upper row) and along-valley wind (lower row) profiles along $x = 0$ km **a)** at the plain $y = -50$ km **b)** valley entrance $y = 0$ km **c)** mid-way of the valley $y = 50$ km at 15:00-16:00 on the first day of the simulation.

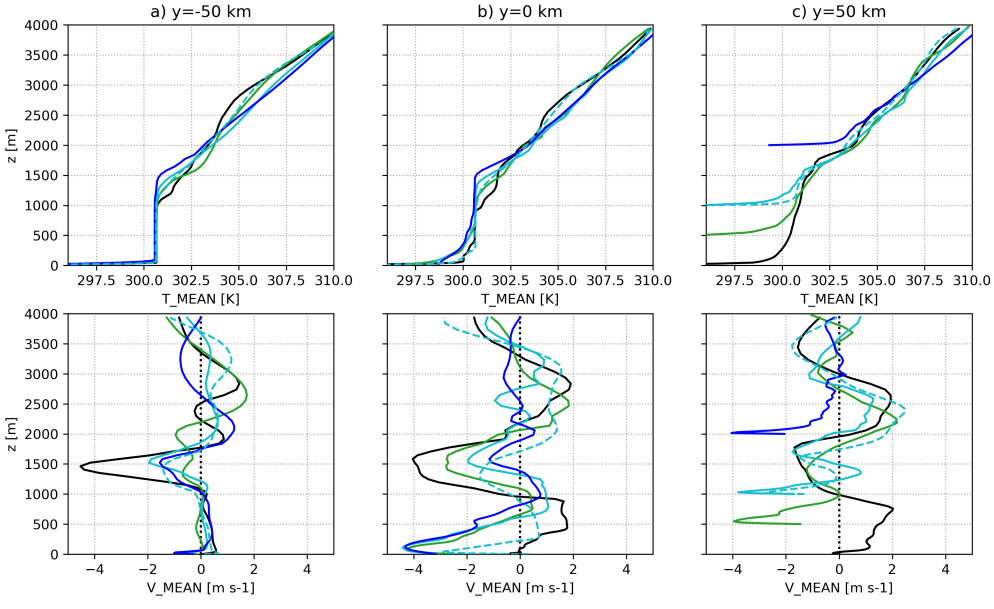

Figure A7. Same as Supplementary Figure A6 but at 03:00-04:00 on the first night of the simulation.

https://doi.org/10.5194/egusphere-2024-1900
Preprint. Discussion started: 15 July 2024

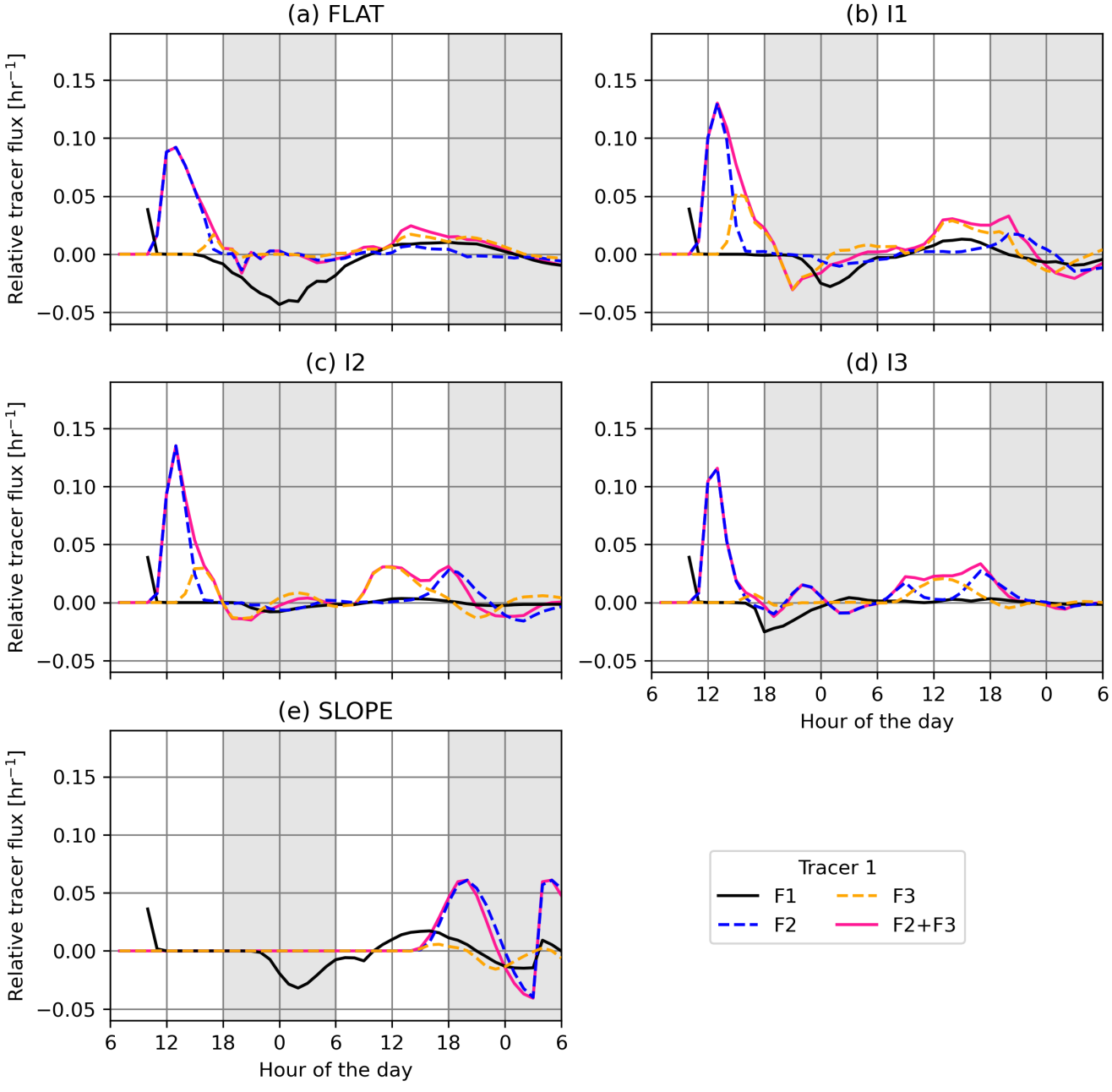

Figure A8. Same as Fig. 8 but for tracer 1

https://doi.org/10.5194/egusphere-2024-1900
Preprint. Discussion started: 15 July 2024

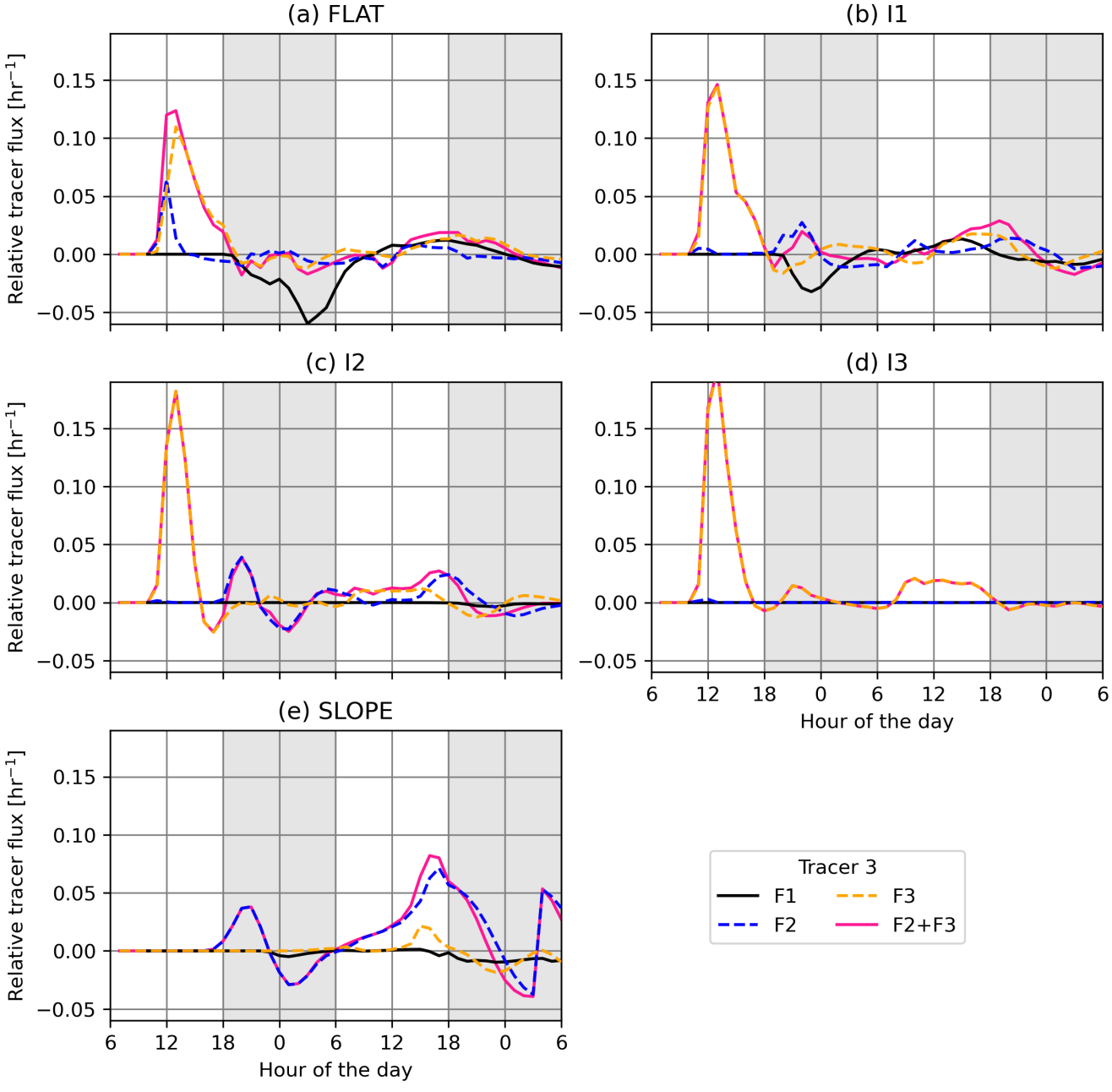

Figure A9. Same as Fig. 8 but for tracer 3

https://doi.org/10.5194/egusphere-2024-1900
Preprint. Discussion started: 15 July 2024

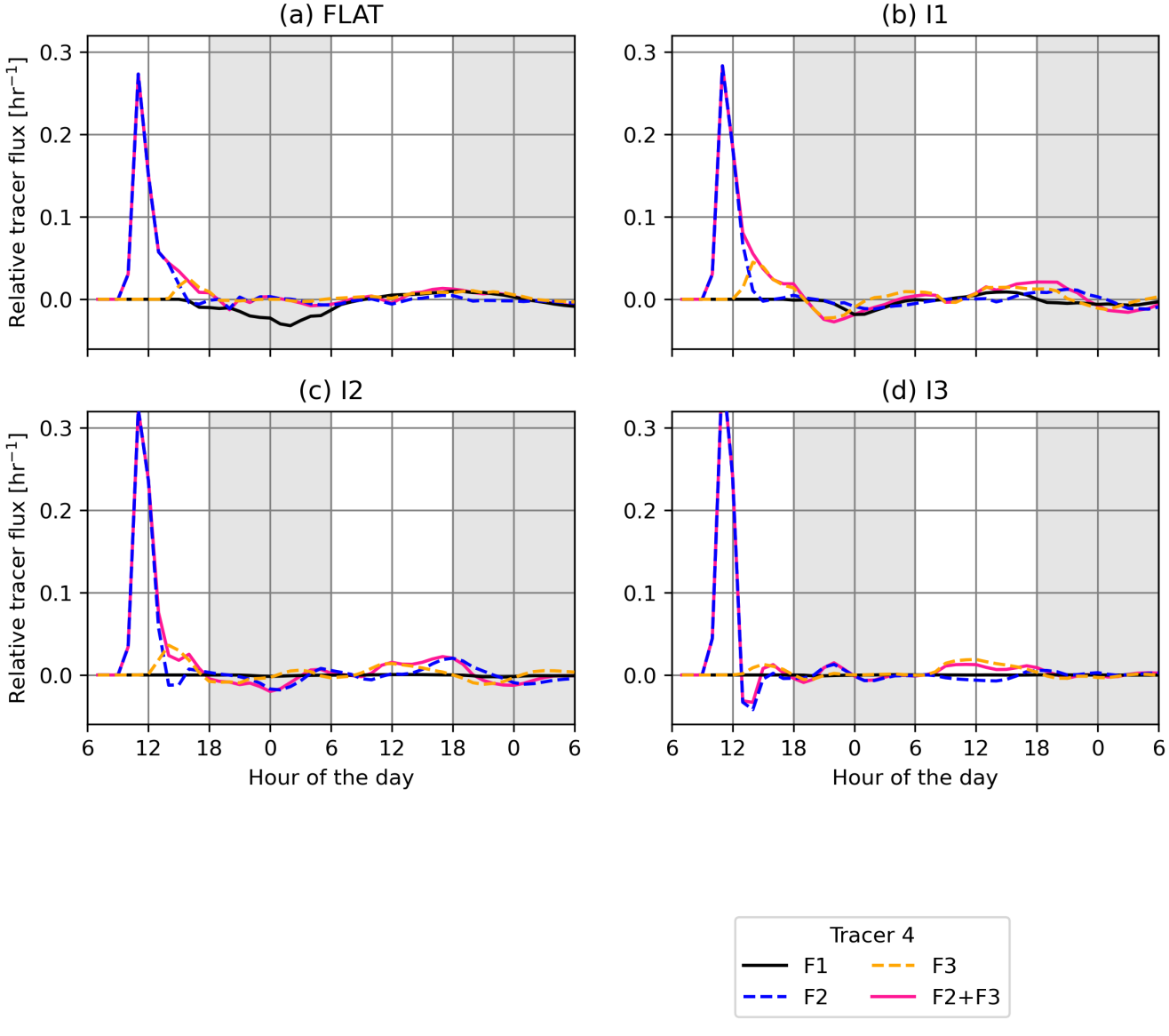

Figure A10. Same as Fig. 8 but for tracer 4. Note that the y-scale is different compared to Figures 8 and Supplementary Figures A4–A5.